LJMU Research Online

Oppenheimer, BD, Segers, M, Schaye, J, Richings, AJ and Crain, RA

 Flickering AGN can explain the strong circumgalactic O VI observed by COS-Halos

http://researchonline.ljmu.ac.uk/id/eprint/8016/

Article

Flickering AGN can explain the strong circumgalactic O VI observed by COS-Halos

Benjamin D. Oppenheimer,[1]⋆ Marijke Segers,[2] Joop Schaye,[2] Alexander J. Richings[3] and Robert A. Crain[4]

[1]*CASA, Department of Astrophysical and Planetary Sciences, University of Colorado, 389 UCB, Boulder, CO 80309, USA*
[2]*Leiden Observatory, Leiden University, PO Box 9513, NL-2300 RA Leiden, the Netherlands*
[3]*Department of Physics and Astronomy and CIERA, Northwestern University, 2145 Sheridan Road, Evanston, IL 60208, USA*
[4]*Astrophysics Research Institute, Liverpool John Moores University, 146 Brownlow Hill, Liverpool L3 5RF, UK*

ABSTRACT

Proximity zone fossils (PZFs) are ionization signatures around recently active galactic nuclei (AGNs) where metal species in the circumgalactic medium remain overionized after the AGNs have shut off due to their long recombination time scales. We explore cosmological zoom hydrodynamic simulations, using the EAGLE (Evolution and Assembly of GaLaxies and their Environments) model paired with a non-equilibrium ionization and cooling module including time-variable AGN radiation to model PZFs around star-forming disc galaxies in the $z \sim 0.2$ Universe. Previous simulations typically underestimated the O VI content of galactic haloes, but we show that plausible PZF models increase O VI column densities by $2 - 3 \times$ to achieve the levels observed around COS-Halos star-forming galaxies out to 150 kpc. Models with AGN bolometric luminosities $\gtrsim 10^{43.6}\mathrm{erg\,s^{-1}}$, duty cycle fractions $\lesssim 10\,\mathrm{per\,cent}$, and AGN lifetimes $\lesssim 10^{6}$ yr are the most promising, because their supermassive black holes grow at the cosmologically expected rate and they mostly appear as inactive AGN, consistent with COS-Halos. The central requirement is that the typical star-forming galaxy hosted an active AGN within a time-scale comparable to the recombination time of a high metal ion, which for circumgalactic O VI is $\approx 10^{7}$ yr. H I, by contrast, returns to equilibrium much more rapidly due to its low neutral fraction and does not show a significant PZF effect. O VI absorption features originating from PZFs appear narrow, indicating photoionization, and are often well aligned with lower metal ion species. PZFs are highly likely to affect the physical interpretation of circumgalactic high ionization metal lines if, as expected, normal galaxies host flickering AGN.

Key words: galaxies: formation – intergalactic medium – quasars: absorption lines – galaxies: Seyfert – cosmology: theory.

1 INTRODUCTION

The circumgalactic medium (CGM) contains a significant reservoir of gaseous baryons extending to the virial radius and beyond. Observations by the Cosmic Origins Spectrograph (COS) show the gas is enriched with heavy elements out to galactocentric radii of at least 150 kpc, as indicated by metal ion absorption features including O VI. By targeting the CGM of star-forming redshift $z \sim 0.2$ galaxies, the COS-Halos survey found very strong O VI, with an average column density $N_{\mathrm{O\,VI}} = 10^{14.6}$ cm^{-2} (Tumlinson et al. 2011).

The estimated circumgalactic reservoir of O VI, in excess of 2×10^{6} M$_\odot$ (Peeples et al. 2014), indicates significant enrich-

ment by galactic superwinds. Cosmological hydrodynamic simulations have been unable to reproduce the typical O VI columns observed around star-forming galaxies. The latest simulations confronting COS-Halos, whether using smoothed-particle hydrodynamics (SPH; Ford et al. 2016; Gutcke et al. 2017), adaptive mesh refinement (Hummels et al. 2013), or moving mesh (Suresh et al. 2017), all seem to fall short by a factor of ≈ 3. These simulations generate O VI column densities of $\approx 10^{14.0}$ cm^{-2} around star-forming L^{*} galaxies with stellar masses $M_* = 10^{10.0}$–$10^{10.5}$ M$_\odot$.

Oppenheimer et al. (2016, hereafter Opp16) also ran a set of zoom simulations using the Evolution and Assembly of GaLaxies and their Environments (EAGLE; Schaye et al. 2015) model, reproducing the observed bimodal correlation of O VI column density with galactic specific star formation rate (sSFR; Tumlinson et al. 2011). While these were the first cosmological

hydrodynamic simulations of galaxies to integrate non-equilibrium (NEQ) ionization and cooling following 136 ions across 11 elements (Oppenheimer & Schaye 2013a), they too find O VI was too weak around L^* galaxies. The NEQ ion-by-ion cooling and abundances under a slowly evolving, spatially uniform ionizing extragalactic background (EGB) does not significantly affect O VI column densities. Hence, circumgalactic O VI in this case is well approximated as being in ionization equilibrium and is found to be too weak.

However, Opp16 did not consider the case of a fluctuating ionization field, such as that arising from a time-variable active galactic nucleus (AGN). Oppenheimer & Schaye (2013b, hereafter OS13) introduced the concept of AGN proximity zone fossils (or PZFs), where an AGN ionizes circumgalactic gas and subsequently turns off, leaving metals in the CGM overionized for a time-scale set by their recombination rate. Segers et al. (2017, hereafter Seg17) were the first paper to simulate PZFs in a cosmological hydro simulation. Using individual haloes selected from the EAGLE simulation, Seg17 performed a parameter exploration of AGN strength and lifetime, duty cycle, halo mass, and redshift, finding that the PZF effect could maintain the column densities of high ions (including O VI) significantly above the equilibrium values for much longer than the AGN lifetime. A galaxy's CGM would appear ionized by an AGN despite the central galaxy showing no signatures of AGN activity.

The key requirement for the PZF effect to be significant is that the recombination time-scale (t_{rec}) to the observed ionization state should be similar to, or longer than, the time between AGN episodes. For a typical CGM density, $n_H = 10^{-4}$ cm^{-3}, the recombination time to O VI is $t_{rec} \sim 10^7$ yr. This may seem short compared to the H I recombination time of 10^9 yr at the same density, but the critical difference is that circumgalactic hydrogen is highly ionized with a neutral fraction $\approx 10^{-4}$, which reduces the time-scale to re-equilibrate to $\approx 10^{-4} \times t_{rec, H I} \sim 10^5$ yr. By contrast, metal ions have fractions for individual ions of order unity, so the full recombination time-scale applies. Therefore, the traditional method of identifying a proximity zone using ionized H I around an active quasar (e.g. Scott et al. 2000) does not apply for PZFs. OS13 argued, and Seg17 demonstrated, that PZFs should be identified as having H I levels consistent with being in equilibrium with the EGB, while metal ions still show signatures of being ionized by the AGN.

Here, we extend the work of Seg17 to argue that PZFs could be common around COS-Halos $z \sim 0.2$ star-forming galaxies. The COS-Halos sample includes no active AGN (Werk et al. 2012), while circumgalactic H I is copious (Thom et al. 2012; Tumlinson et al. 2013). Our argument for O VI enhanced by PZFs hinges on the assumption that many of these galaxies were AGN within the recent past, defined roughly as $t_{rec, O VI}$. AGN lifetimes are typically inferred to be $t_{AGN} \sim 10^6$–10^8 yr (e.g. Haiman & Hui 2001; Martini & Weinberg 2001; Jakobsen et al. 2003; Schirber, Miralda-Escudé & McDonald 2004; Hopkins et al. 2006; Gonçalves, Steidel & Pettini 2008), but these measurements constrain duty cycle, and individual AGN-on episodes could be much shorter. We additionally explore $t_{AGN} \sim 10^5$ yr here, which is motivated by arguments including those of Gabor & Bournaud (2013) and Schawinski et al. (2015) that supermassive black holes (SMBHs) flicker with shorter, luminous AGN-on phases.

OS13 showed that the most important parameter for PZF enhancement is the average interval between AGN episodes, which is a combination of t_{AGN} and duty cycle fraction (f_{duty}), or approximately t_{AGN}/f_{duty}. Seg17 demonstrated that short, flickering AGN-on phases create stronger PZF effects than a single, longer AGN-on phase, because t_{rec} remains the same as long as the AGN can ionize the CGM within a single burst. Additionally, subsequent AGN-on phases can accumulate to raise the ionization state of the CGM, further enhancing the PZF effect (OS13; Seg17). Hence, the PZF effect can non-linearly enhance metal ions in the CGM if an AGN flickers.

AGN light echoes, where an AGN recently shut off or became obscured along the line of sight (LOS) to the object but leave the surrounding CGM at an enhanced ionization level, may be observations of on-going PZF effects. Lintott et al. (2009) found enhanced [O III] out to 27 kpc from IC 2497, discovered in Galaxy Zoo as 'Hanny's Voorwerp' and suggesting a change in AGN activity within the last 10^5 yr. The enhanced oxygen ionization may be a direct example of the PZF effect, albeit in higher density gas that can be detected in emission. Bland-Hawthorn et al. (2013) argued that a 'Seyfert flare' in our own Galaxy 1–3 Myr ago, which also formed the *Fermi* bubble observed from Sgr A*, could be responsible for the strong H α observed in the Magellanic Stream. Schirmer et al. (2016) discovered 14 Ly α blobs at $z \approx 0.3$ that appear to be associated with flickering AGN that have faded in the X-ray by a factor of 10^{3-4} in the last 10^{4-5} yr. These three examples may be PZF effects that are detected in emission, but our exploration focuses on quasar absorption lines probing more diffuse, more highly ionized CGM gas.

The paper is organized as follows. We describe our zoom simulations and the implementation of AGN fluctuations into the NEQ ionization module included in the GADGET-3-based EAGLE code in Section 2. We next consider the latest observational and theoretical results regarding how SMBHs grow in low-redshift star-forming galaxies in Section 3. Our main results are presented in Section 4, and we discuss their implications in Section 5. We summarize in Section 6.

2 SIMULATIONS

We use the EAGLE simulation code described by Schaye et al. (2015, hereafter Sch15) and Crain et al. (2015), which is an extensively modified version of the N-body+SPH code GADGET-3 last described by Springel (2005). EAGLE includes calibrated prescriptions for star formation, stellar evolution and chemical enrichment, and superwind feedback associated with star formation and the SMBH growth. Because EAGLE successfully reproduces an array of stellar and cold ISM properties of galaxies across a Hubble time (e.g. Sch15; Furlong et al. 2015; Lagos et al. 2015; Trayford et al. 2015; Bahé et al. 2016; Segers et al. 2016; Crain et al. 2017), while following the hydrodynamics, it represents an ideal test bed for the study of the physical state of the gaseous intergalactic medium (IGM) and the CGM. Absorption line statistics probing the IGM are examined by Rahmati et al. (2015) for H I and by Rahmati et al. (2016) for metal ions, showing broad agreement with observations, although notably an underestimate of O VI absorber frequency for $N_{O VI} \gtrsim 10^{14.5}$ cm^{-2} at $z \approx 0$–0.5. Rosas-Guevara et al. (2016) explored AGN and SMBH statistics in EAGLE finding excellent agreement with observations between $z = 0$ and 1, and McAlpine et al. (2017) demonstrated EAGLE reproduces the observed relationships between galaxy star formation rate (SFR) and SMBH accretion rate. The underestimates of strong O VI absorbers in Rahmati et al. (2016) and Opp16 provide motivation for this work.

2.1 Non-equilibrium network

Opp16 ran a set of high-resolution EAGLE zooms focusing on the CGM of $z \sim 0.2$ galaxies similar to those observed by COS-Halos. These simulations include the NEQ solver introduced by Oppenheimer & Schaye (2013a), and integrated into the EAGLE code as described in Opp16. The NEQ module explicitly solves the reaction network of 136 ionization states for 11 elements that contribute most significantly to radiative cooling. The module replaces the equilibrium cooling module of Wiersma, Schaye & Smith (2009), which enables a self-consistent transition from equilibrium to NEQ runs at a specified redshift. The reaction network includes radiative and di-electric recombination, collisional ionization, photoionization, Auger ionization, and charge transfer, as well as ion-by-ion cooling (Gnat & Ferland 2012; Oppenheimer & Schaye 2013a). The NEQ module is activated only at late times ($z = 0.5$ or $z = 0.28$ in the Opp16 zooms), because of its significant computational expense. Opp16 follow the NEQ network in all non-star-forming gas (i.e. the IGM/CGM), but do not follow the ISM NEQ behaviour and chemistry described by Richings, Schaye & Oppenheimer (2014). We also do not follow the effects of AGN radiation on the ISM.

In Opp16, the NEQ effects were found to be minimal for O VI CGM column densities under a slowly evolving EGB field, modelled using the Haardt & Madau (2001) quasar+galaxy background. Additionally, the dynamics of the gas and the appearance of the galaxies did not differ significantly between NEQ and equilibrium runs.

2.2 Fluctuating AGN implementation

Here, we add to the NEQ module the capability of adding a spatially and temporally variable ionizing field, corresponding to localized ionization by an AGN. We assume that the Haardt & Madau (2001) EGB is always present, and add the ionizing spectrum derived by Sazonov, Ostriker & Sunyaev (2004) for unobscured AGN. This is the same spectrum used by Seg17 and is shown in their fig. 3. We have calculated the photoionization rates, $\Gamma_{x_i,\mathrm{AGN}}$, for ionization state i of atomic species x for the Sazonov spectrum using

$$\Gamma_{x_i,\mathrm{AGN}} = \int_{\nu_{0,x_i}}^{\infty} \frac{f_\nu}{h\nu} \sigma_{x_i}(\nu)\mathrm{d}\nu, \tag{1}$$

where ν is frequency, ν_{0,x_i} is the ionization frequency, f_ν is the flux from the AGN, $\sigma_{x_i}(\nu)$ is photoionization cross-section, and h is the Planck constant. Our NEQ module uses the Sundials CVODE[1] solver to integrate the ionization balance over a hydrodynamic timestep, according to it

$$\frac{\mathrm{d}n_{x_i}}{\mathrm{d}t} = n_{x_{i+1}}\alpha_{x_{i+1}}n_e + n_{x_{i-1}}(\beta_{x_{i-1}}n_e + \Gamma_{x_{i-1},\mathrm{EGB}}$$
$$+ \Gamma_{x_{i-1},\mathrm{AGN}}) - n_{x_i}((\alpha_{x_i} + \beta_{x_i})n_e + \Gamma_{x_i,\mathrm{EGB}} + \Gamma_{x_i,\mathrm{AGN}}), \tag{2}$$

where n is the particle number density (cm^{-3}) for a given x_i ionization state, n_e is the free electron density (cm^{-3}), α_{x_i} is the total recombination rate coefficient (radiative plus di-electric, cm^3 s^{-1}), and β_{x_i} is the collisional ionization rate coefficient (cm^3 s^{-1}).

We modify the EAGLE GADGET-3 code to calculate $\Gamma_{x_i,\mathrm{AGN}}$ for each gas particle based on its distance from the central SMBH. We do not attempt to link AGN activity self-consistently to the simulated accretion rate of the central SMBH. Instead, we explore a variety of AGN time histories based on several parameters including

[1] https://computation.llnl.gov/casc/sundials/main.html

luminosity (L_{bol}), AGN lifetime (t_{AGN}, i.e. the length of time the AGN is on), and duty cycle fraction (f_{duty}). We set t_{AGN} by the timestep length over which all SPH particles are updated, which is adjusted by setting the GADGET-3 parameter for the maximum hydro timestep. A random number generator determines if the AGN is on according to fraction f_{duty} at each such correlated timestep. This stochastic AGN flickering differs from the constant interval between AGN episodes explored by Seg17.

A simulation with $t_{\mathrm{AGN}} = 10^5$ yr takes a much longer run time than one adopting $t_{\mathrm{AGN}} = 10^7$ yr, because every particle is updated on this short correlated timestep. GADGET-3 uses differential timestepping and a normal run updates only the densest particles on a $\lesssim 10^5$ yr timestep at our zoom resolution. The hydro performance is essentially the same by resetting the maximum hydro timestep to a smaller value, but more hydro timesteps are taken to track the radiation field for shorter t_{AGN}. We explore timesteps of $10^{5.0}$, $10^{6.2}$, and $10^{7.1}$ yr, which are slightly out-of-sync with 1.0 dex steps owing to GADGET-3's time-stepping.

We do not perform radiative transfer calculations of the propagation of AGN photons. We simply turn on an AGN at a given timestep and do not consider light travel time effects, which we argue in Section 5 is reasonable for our exploration. While our main models emit AGN radiation isotropically, we also explore biconical opening angles for the AGN radiation. Photoheating from the AGN radiation is included in these runs, although it is dynamically and observationally unimportant as shown by OS13 and Seg17. These are the first dynamic simulation runs we know of with NEQ ionization and cooling including fluctuating AGN. Vogelsberger et al. (2013) integrated radiative AGN feedback into AREPO simulations, but their assumption of ionization equilibrium precludes the PZF effect.

Finally, we note that our method of using dynamic EAGLE zoom runs recovers the same results as the Seg17 method of using a halo from a static snapshot. For this test, we applied both methods to a $z = 0.1$ zoom of a $M_* = 2 \times 10^{10}\,\mathrm{M}_\odot$ galaxy and verified that (1) O VI, C IV, and H I as functions of impact parameter and time agreed, and (2) the ionization histories for individual gas particles agreed.

2.3 Zoom simulations

The zoom simulation method is presented in section 2.3 of Opp16, and we briefly describe some details here. We use the zoom initial condition generation methods described by Jenkins (2010) and Jenkins & Booth (2013). Planck Collaboration I (2014) cosmological parameters as adopted by EAGLE are $\Omega_{\mathrm{m}} = 0.307$, $\Omega_\Lambda = 0.693$, $\Omega_b = 0.04825$, $H_0 = 67.77\,\mathrm{km\,s^{-1}\,Mpc^{-1}}$, $\sigma_8 = 0.8288$, and $n_s = 0.9611$. We choose one target halo for re-simulation from the EAGLE Recal-L025N0752 simulation, and particles are identified at $z = 0$ in a spherical region with radius $3R_{200}$ (where R_{200} encloses an overdensity of $200 \times$ the critical overdensity).

We select the Gal001 halo listed in table 1 of Opp16 for our exploration of the AGN PZF effect. In contrast to Opp16, who used a set of 20 zoom simulations to simulate the star-forming and passive COS-Halos sample, we limit our exploration to a single zoom applied to the star-forming sample. This zoom shows typical O VI columns of the Opp16 star-forming blue galaxy sample (see Section 4), meaning we can use it as the baseline comparison for the PZF effect. The primary zoom resolution is *M5.3*, where the resolution nomenclature refers to SPH particle mass resolution according to $M[\log(m_{\mathrm{SPH}}/\mathrm{M}_\odot)]$. At $z = 0.2$, the halo mass is $M_{200} = 10^{12.07}\,\mathrm{M}_\odot$, the central galaxy stellar mass is $M_* = 10^{10.27}\,\mathrm{M}_\odot$, and the SFR is $1.4\,\mathrm{M}_\odot\,\mathrm{yr}^{-1}$ in the run without

Table 1. Zoom simulation runs with flickering AGN.

Name	Resolution[a]	$f_{\text{th, max}}$	$f_{\text{th, min}}$	$C_{\text{visc}}/2\pi$	log M_{200}^{b} (M$_\odot$)	log M_*^{b} (M$_\odot$)	SFR[b] (M$_\odot$ yr^{-1})	M_{BH}^{b} (M$_\odot$)
Gal001	*M5.3*	3.0	0.3	10^3	12.07	10.27	1.426	$10^{7.06}$
Gal001	*M4.4*	2.0	0.3	10^4	12.09	10.28	1.791	$10^{6.85}$

Notes. [a]$M[\log_{10}(m_{\text{SPH}}/\text{M}_\odot)]$,
[b]at $z = 0.205$.

radiative AGN activity. The softening is 350 proper pc at $z < 2.8$. This zoom simulates a typical star-forming L^* galaxy using the EAGLE-'Recal' prescription described by Sch15. This object is an intermediate mass L^* galaxy from Opp16, and its properties, as well as the EAGLE-Recal prescription feedback parameters, are listed in Table 1. The run without AGN radiative activity from Opp16 is termed the No-AGN-Rad run.

We also simulate the Gal001 halo at $8 \times$ higher mass resolution, *M4.4*, to test resolution convergence in Appendix A. This is run in equilibrium from $z = 127$ with a modified feedback prescription to compensate for the fact that stellar masses at *M4.4* resolution were 0.18 dex lower using the EAGLE-Recal prescription (Opp16). The EAGLE strategy is to recalibrate the subgrid models at different resolutions as described by Sch15, which was not done in Opp16 for *M4.4* zooms. Here, we take the EAGLE-Recal prescription and reduce the stellar feedback energy by lowering the parameter $f_{\text{th, max}}$ of Sch15 from 3.0 to 2.0, and reducing the viscosity of gas accreting on to the SMBH by raising the C_{visc} parameter that scales inversely with subgrid viscosity (Rosas-Guevara et al. 2015) from $2\pi \times 10^3$ to $2\pi \times 10^4$. The result is a galaxy with a similar stellar mass as the *M5.3* run, and a similar albeit slightly lower mass black hole at the centre (see Table 1).

Finally, we run a set of *M5.3* models with the AGN turned on to demonstrate the expectations of constant AGN radiation on the CGM. This is not applicable to COS-Halos, but could be applicable to a survey targeting sight lines around active AGN, including the COS-AGN survey (Berg et al. in preparation). We present the O VI results in the Appendix B.

2.4 Running in non-equilibrium

Simulations are run with NEQ ionization and cooling from $z = 0.271$, and AGN fluctuations begin between $z = 0.230$ and 0.225. Because we compare to the COS-Halos observations centred at $z \sim 0.2$, we focus our AGN fluctuation snapshots around this redshift, usually running simulations to $z = 0.15$.

We parametrize AGN luminosity using L_{bol}, exploring the interval $\log[L_{\text{bol}}/(\text{erg s}^{-1})] = 43.1\text{--}45.1$, which corresponds to Eddington ratios,

$$\lambda_{\text{Edd}} \equiv \frac{L_{\text{bol}}}{L_{\text{Edd}}} \tag{3}$$

ranging between 10^{-2} and 1 for $M_{\text{BH}} = 10^{7.0}$ M$_\odot$. We assume $10^{7.0}$ M$_\odot$ when quoting Eddington ratios, and we do not adjust bolometric luminosities based on the SMBH mass, which differs between *M5.3* and *M4.4* resolutions and increases slightly over our explored redshift interval. These SMBH masses are typical in the EAGLE cosmological volumes where the median SMBH mass is 10^7 M$_\odot$ for a 10^{12} M$_\odot$ halo at $z = 0.0$ (Rosas-Guevara et al. 2016).

We output high-cadence 'snapshots', which are abbreviated EAGLE snapshots with fewer fields and only a handful of NEQ ions. Snapshots are output every 4 Myr for a total of 234 between $z = 0.23$ and 0.15. For most of the $t_{\text{AGN}} = 10^5$ yr runs, we only

run to just below $z = 0.20$ owing to the greater expense of these runs. However, there is no statistical difference in O VI columns in a No-AGN-Rad run between $z = 0.23 \rightarrow 0.19$ and $z = 0.23 \rightarrow 0.15$.

2.5 Observational sample selection

We take the subset of the COS-Halos blue, star-forming galaxies defined as having sSFR greater than 10^{-11} yr^{-1} and stellar masses between $10^{9.8}$ and $10^{10.5}$ M$_\odot$ using a Chabrier (2003) IMF. This leaves 20 galaxies with a median sSFR = $10^{-10.0}$ yr^{-1} using the catalogue of Werk et al. (2013). The observed median O VI column density is $10^{14.57}$ cm^{-2} for impact parameters $b = 20\text{--}140$ kpc. The additional six galaxies in the COS-Halos blue sample with $M_* > 10^{10.5}$ M$_\odot$ have slightly lower sSFR and lower O VI columns including two upper limits below $10^{14.0}$ cm^{-2} and a median value of $10^{14.38}$ cm^{-2}. The redshift range of the observed sample is $z = 0.14\text{--}0.36$, with a median of $z = 0.22$.

Our simulated *M5.3* central galaxy with $M_* = 10^{10.3}$ M$_\odot$ and sSFR = $10^{-10.1}$ yr^{-1} is representative of the COS-Halos blue subset. We explore a limited redshift range, but one which includes the median redshift of the observed sample. Opp16 found no significant dependence of O VI column densities on redshift.

3 EXPERIMENT DESIGN RATIONALE

Our hypothesis that the PZF effect boosts the COS-Halos O VI column densities relies on the majority of COS-Halos star-forming galaxies hosting AGN luminous enough to have ionized the CGM in the recent past, which is defined as the lifetime of the PZF set by the recombination time-scale to the given metal ion. OS13 and Seg17 show that t_{rec} for O VI is 5–10 Myr at typical $z \sim 0.2$ CGM densities, which means that most of the COS-Halos blue sample should have hosted a luminous AGN within this time-scale. Another requirement is that the AGN are infrequent enough that it is statistically plausible that none of the COS-Halos blue galaxies appear as active AGN, because none of them appear as such according to Werk et al. (2012). Finally, the AGN luminosities, lifetimes, and duty cycles need to be 'evolutionarily sustainable', such that the implied SMBH growth rates are reasonable for a typical star-forming galaxy, and therefore cosmologically expected. The hypothesis would fail if we required many of the 20 observed galaxies to be undergoing a rare stage of SMBH growth. We now consider recent observations and theoretical results regarding AGN and SMBH growth in low-redshift, low-luminosity AGN.

3.1 AGN luminosities and duty cycles in star-forming galaxies

Our typical SMBH mass is 10^7 M$_\odot$ in a $M_* = 10^{10.3}$ M$_\odot$ galaxy and is representative of EAGLE cosmological volumes (Rosas-Guevara et al. 2016). The observed Häring & Rix (2004) SMBH mass–galaxy mass relation predicts about $\approx 2 \times$ more massive SMBH in their local sample, but it should be noted that this is a bulge-dominated sample. Recent work shows that disc-dominated

galaxies host low-luminosity AGN, which is critical for our hypothesis since COS-Halos star-forming galaxies are disc galaxies. Sun et al. (2015) compiled an X-ray-selected, *Herschel* cross-matched sample of disc-dominated galaxies with AGN calculating a duty cycle of ≈ 10 per cent with an average $\lambda_{Edd} \sim 0.1$.

Eddington ratios range between 0.01 and 1 for typical broad-line quasar activity with the $\lambda_{Edd} \sim 0.01$ lower limit observed by Kollmeier et al. (2006) and Trump et al. (2009). Eddington ratios approaching unity are rare in the low-redshift Universe (e.g. Shen et al. 2008). Such high Eddington ratios are more likely to be associated with *quasar* activity, where an SMBH gains most of its mass in a couple episodes (e.g. Hopkins & Hernquist 2009), but we are considering *Seyfert*-level activity where lower Eddington ratios appear to dominate SMBH growth. Hopkins & Hernquist (2006) developed a stochastic cold-accretion model to fit the Seyfert luminosity function, where 'quiescent' accretion dominates SMBH growth in spiral galaxies with the most likely accretion luminosities having $\lambda_{Edd} \sim 0.01$ and extending up to ~ 0.1 for $M_{BH} = 10^7\,M_\odot$.

Low-luminosity AGN may not always appear as optically selected AGN using a method like the Baldwin, Phillips & Terlevich (1981, BPT) diagnostic as used by Werk et al. (2012). Satyapal et al. (2014) demonstrated that optical selection may miss many AGN in bulgeless galaxies and that infrared *WISE (Wide-field Infrared Survey Explorer)*-selected AGN may be prevalent in star-forming galaxies. Trump et al. (2015) showed that star formation can outshine AGN activity in high-sSFR disc galaxies. It may be that much of the growth of $10^7\,M_\odot$ black holes is shielded from traditional optical identification, although it is not clear what this means for the far-UV spectrum, which is needed to ionize O VI in PZFs.

X-rays have fewer biases than optical detections, and the survey of Haggard et al. (2010) finds 1.2 per cent AGN detection fraction in field galaxies with L^* luminosities, which is consistent with COS-Halos showing no active AGN. However, in the real Universe, AGNs are not on–off light bulbs, and the intrinsic Eddington ratio distribution of star-forming galaxy SMBHs may be best modelled by a power-law distribution with a steep cut-off at $\lambda_{Edd} \gtrsim 0.1$ (Jones et al. 2016; Aird, Coil & Georgakakis 2017).

3.2 AGN lifetimes in star-forming galaxies

Quasar lifetimes are calculated to be $\approx 10^6$–10^8 yr (e.g. Haiman & Hui 2001; Martini & Weinberg 2001) based on quasar clustering and halo occupation, but these measurements constrain total duty cycle fraction and not the duration of individual quasar episodes. Ionization of the surrounding IGM, often probed via the transverse proximity effect of paired quasars, can also be used to indirectly constrain quasar lifetimes to be $\gtrsim 10^7$ yr (Jakobsen et al. 2003; Schirber et al. 2004; Gonçalves et al. 2008; Borisova et al. 2016), but consideration of quasar flickering would require re-interpretation of these results.

Recent results support shorter AGN lifetimes, especially when considering low-luminosity AGN in discs. Schawinski et al. (2015) constrains AGN lifetimes to $\approx 10^5$ yr based on the timing argument that there is a lag between the AGN central engine becoming X-ray active and ionizing its host galaxy's ISM as indicated in optical lines. Hence, the fraction of X-ray bright, optically normal galaxies can be combined with the time lag to argue that AGN flicker in many (100–1000) accretion bursts. The simulations of Gabor & Bournaud (2013) find the accretion of smaller clouds in low-z gas-poor discs leads to shorter AGN phases of 10^5 yr in contrast to longer phases in high-z, gas-rich discs. Other theoretical works considering accretion on pc and sub-pc scales (Novak, Ostriker & Ciotti 2011;

King & Nixon 2015) also indicate chaotic accretion episodes lasting $\approx 10^5$ yr.

3.3 SMBH growth rates in star-forming galaxies

When considering stochastic AGN activity in a sample of star-forming galaxies, one needs to consider the time-averaged rate of growth of the black hole in relation to the growth of the galaxy. The sSFR of the blue COS-Halos sample implies a stellar mass doubling time of 10^{10} yr, which is much longer than the Salpeter (1964) time-scale, $t_{Sal} \equiv M_{BH}/\dot{M}_{Edd} = 4 \times 10^7$ yr, required for an Eddington-limited BH to double in mass assuming a radiative efficiency, $\epsilon_{rad} = 10$ per cent, where $\dot{M}_{Edd} = L_{Edd}/(\epsilon_{rad}c^2)$.

What combinations of duty cycle fraction and sub-Eddington accretion rates are reasonable for SMBH growth in star-forming disc galaxies? Hickox et al. (2014) demonstrate that a model where long-term SMBH accretion rates correlate with SFRs can explain observed AGN statistics. The BH tracks the galaxy growth on a long time-scale, which means the BH growth rate would match the sSFR $= 10^{-10}$ yr^{-1} if the average SMBH growth rate is $t_{Sal} \times$ sSFR $= 0.004$ or 0.4 per cent times the Eddington rate. We consider the time-averaged black hole specific accretion rate,

$$s\dot{M}_{BH} \equiv \frac{\dot{M}_{BH}}{M_{BH}}, \tag{4}$$

when exploring PZF parameters, λ_{Edd}, f_{duty}, and t_{AGN}.

Sun et al. (2015) also find general co-evolution of galaxies and their black holes, which is consistent with no deviation in the M_{BH}/M_* ratio from $z = 2 \rightarrow 0$. However, they specifically find that low-z disc black holes appear to grow faster than their galaxies, often with $s\dot{M}_{BH} > 10^{-9}$ yr^{-1}. The time-averaged λ_{Edd} in EAGLE simulations for a $10^7\,M_\odot$ SMBH at $z = 0$–0.2 is 0.01 (Rosas-Guevara et al. 2016), which translates to $s\dot{M}_{BH} = 2.5 \times 10^{-10}$ yr^{-1} and is at least $2 \times$ higher than the typical sSFR. SMBH masses rapidly increase around $M_{200} = 10^{12}\,M_\odot$ in EAGLE, which appears related to the inability of gas heated by supernova-driven feedback to buoyantly rise through the hot circumgalactic coronae that form at this halo mass (Bower et al. 2017; McAlpine et al. 2017). Inefficient feedback leads to rapid, non-linear growth of the black hole.

We select our AGN models based on all these considerations: AGN luminosities, duty cycles, lifetimes, and evolutionarily sustainable SMBH growth rates. Our models treat AGN as on–off light bulbs in this exploration, even though a power-law distribution for λ_{Edd} may be more appropriate given recent observational results (e.g. Jones et al. 2016) and theoretical work (e.g. Gabor & Bournaud 2013). We may explore such distributions in the future, but we do add a new AGN flickering model based on the recent X-ray-derived accretion rate distributions of Aird et al. (2017), who provide the average Eddington ratio ($\lambda_{Edd} \sim 0.1$) and duty cycle fraction (1 per cent) above $\lambda_{Edd} > 0.01$.

4 FLUCTUATING AGN IONIZING THE CGM OF L^* GALAXIES

We choose our reference AGN model for the PZF effect: $L_{bol} = 10^{44.1}\,erg\,s^{-1}$ ($\lambda_{Edd} = 0.1$), $f_{duty} = 10$ per cent, and $t_{AGN} = 10^{6.2}$ yr. This model, referred to as *L441d10t6* using the nomenclature $L[\log(L_{bol}/erg\,s^{-1}) \times 10]d[f_{duty}$ per cent]$t[\log(t_{AGN}$ yr$^{-1})]$ and listed in bold in Table 2, has an $s\dot{M}_{BH} = 2.5 \times 10^{-10}$ yr^{-1} matching the time-averaged SMBH growth rate in EAGLE. Most models we explore have lower $s\dot{M}_{BH}$ because (1) we want to explore the minimum requirements for PZFs and (2) the required

Table 2. Proximity zone fossils models.

Name	Resolution	L_{bol}^a	f_{duty}	t_{AGN}^b	$s\dot{M}_{BH}^c$	Isotropic?	$N_{O\,VI,0-75}^{d,e}$	$N_{O\,VI,75-150}^{d,f}$
No-AGN-Rad	*M5.3*	–	–	–	–	–	$14.19^{+0.15}_{-0.15}$	$14.17^{+0.15}_{-0.17}$
L441d10t6	*M5.3*	44.1	10	6.2	2.5×10^{-10}	Yes	$14.62^{+0.42}_{-0.32}$	$14.42^{+0.26}_{-0.23}$
L441d10t7	*M5.3*	44.1	10	**7.1**	2.5×10^{-10}	Yes	$14.36^{+0.38}_{-0.21}$	$14.30^{+0.26}_{-0.21}$
L441d10t5	*M5.3*	44.1	10	**5.0**	2.5×10^{-10}	Yes	$14.89^{+0.28}_{-0.30}$	$14.47^{+0.20}_{-0.21}$
L431d10t6	*M5.3*	**43.1**	10	6.2	2.5×10^{-11}	Yes	$14.33^{+0.23}_{-0.19}$	$14.20^{+0.15}_{-0.17}$
L436d10t6	*M5.3*	**43.6**	10	6.2	8×10^{-11}	Yes	$14.43^{+0.30}_{-0.24}$	$14.29^{+0.16}_{-0.19}$
L451d10t6	*M5.3*	**45.1**	10	6.2	2.5×10^{-9}	Yes	$14.84^{+0.35}_{-0.38}$	$14.67^{+0.38}_{-0.34}$
L441d01t5	*M5.3*	44.1	**1.0**	**5.0**	2.5×10^{-11}	Yes	$14.32^{+0.21}_{-0.16}$	$14.23^{+0.14}_{-0.18}$
L441d03t5	*M5.3*	44.1	**3.2**	**5.0**	8×10^{-11}	Yes	$14.63^{+0.28}_{-0.27}$	$14.32^{+0.15}_{-0.18}$
L441d03t6	*M5.3*	44.1	**3.2**	6.2	8×10^{-11}	Yes	$14.35^{+0.37}_{-0.21}$	$14.28^{+0.20}_{-0.20}$
L431d32t6	*M5.3*	**43.1**	**32**	6.2	8×10^{-11}	Yes	$14.50^{+0.27}_{-0.20}$	$14.30^{+0.16}_{-0.20}$
L446d01t5	*M5.3*	**44.6**	**1.0**	**5.0**	8×10^{-11}	Yes	$14.62^{+0.47}_{-0.29}$	$14.33^{+0.19}_{-0.20}$
L436d10t5	*M5.3*	**43.6**	10	**5.0**	8×10^{-11}	Yes	$14.59^{+0.27}_{-0.24}$	$14.30^{+0.17}_{-0.24}$
L431d32t5	*M5.3*	**43.1**	**32**	**5.0**	8×10^{-11}	Yes	$14.64^{+0.25}_{-0.27}$	$14.33^{+0.15}_{-0.19}$
L441d10t6-bicone	*M5.3*	44.1	10	6.2	2.5×10^{-10}	**Biconical**	$14.45^{+0.36}_{-0.26}$	$14.32^{+0.23}_{-0.21}$
L441d10t5-bicone	*M5.3*	44.1	10	**5.0**	2.5×10^{-10}	**Biconical**	$14.66^{+0.35}_{-0.34}$	$14.34^{+0.23}_{-0.23}$
No-AGN-Rad-*M4.4*	*M4.4*	–	–	–	–	–	$14.33^{+0.16}_{-0.14}$	$14.36^{+0.15}_{-0.15}$
L441d10t6-M4.4	*M4.4*	44.1	10	6.2	2.5×10^{-10}	Yes	$14.54^{+0.26}_{-0.20}$	$14.48^{+0.17}_{-0.1}$
L441d10t5-M4.4	*M4.4*	44.1	10	**5.0**	2.5×10^{-10}	Yes	$14.75^{+0.32}_{-0.21}$	$14.57^{+0.10}_{-0.19}$
COS-Halos	–	–	–	–	–	–	$14.71^{+0.24}_{-0.15}$	$14.52^{+0.14}_{-0.18}$

Notes. ^{a}Log erg s^{-1},
^{b}log yr,
^{c} yr^{-1},
^{d} cm^{-2},
^{e}0–75 kpc,
^{f}75–150 kpc.

parameter choices prefer lower $s\dot{M}_{BH}$, because first we want duty cycle fractions to be small so that most star-forming galaxies do not appear as AGN, and second Eddington-limited accretion is rare at low-z. Seg17 performed a similar parameter exploration, using parameters λ_{Edd} (spanning 0.01–1), f_{duty} (spanning 1–50 per cent), and t_{AGN} (spanning 10^5–10^7 yr plus considering 10^3–10^5 yr for a special case). Seg17 also performed a wider parameter exploration, considering multiple redshift ($z = 3.0, 0.1$) and galaxy masses ($M_* = 10^{10}, 10^{11}$ M$_\odot$), whereas we are applying PZFs to COS-Halos star-forming galaxies.

We present our main results in this section, beginning with the PZF effect assuming isotropic emission and varying the parameters L_{bol}, t_{AGN}, and f_{duty}. We then extend our analyses to models with anisotropic emission.

4.1 Isotropic models

The evolutions of $N_{H\,I}$ and $N_{O\,VI}$, in the No-AGN-Rad model and our reference model, *L441d10t6*, are plotted in the upper set of panels of Fig. 1. We show 380 Myr histories of the median H I (upper panels) and O VI (middle panels) column densities in three impact parameter bins ($b = 0$–50, 50–100, and 100–150 kpc). The O VI column densities in the No-AGN-Rad model (left) are too weak by a factor of 2–3, showing little variation with time. The *L441d10t6* panels (right) span 34 AGN-on phases lasting 1.5 Myr each, which are indicated by a dip in H I and a spike in O VI. The H I returns rapidly to its equilibrium ionization level on a time-scale of $\approx 10^5$ yr, which is too short to be seen on this plot. O VI, on the other hand, shows a prolonged decline for every AGN-on phase,

illustrating how the delayed recombination effect occurs for metal ions but not H I.

We show three sets of H I and O VI column density maps in the lower portion of Fig. 1 to illustrate the general behaviour of PZFs. The column density maps are 600×600 kpc across with 1 kpc pixel sizes, which we find to be converged with the column densities being insensitive to pixel size at this size and smaller. The first snapshots at $z = 0.23$ (left) show a normal CGM unaffected by the AGN. We display an AGN-on phase just below $z = 0.20$ in the middle panels, where H I is diminished and O VI is enhanced, especially in the inner 100 kpc. The right-hand panel shows the CGM 4 Myr after the AGN turns off, when H I has returned to its earlier appearance, but O VI is still enhanced due to the delayed recombination PZF effect.

To compare directly with the COS-Halos blue galaxy sample, we use the PYTHON module called Simulation Mocker Of Hubble Absorption-Line Observational Surveys (SMOHALOS) introduced by Opp16 to create mock COS-Halos surveys using the observed impact parameters of that survey. Unlike Opp16, who used 20 zooms at six different redshifts to find the simulated galaxy that matched the observed galaxy most closely in terms of M_* and sSFR, here we use one evolving zoom at every redshift output between $z = 0.225$ and 0.15 where the AGN is off, which gives us 193 out of 213 snispshot. Mock column densities are selected from column density maps along the *x*, *y*, and *z* projections with 1 kpc pixel resolution, which we tested for resolution convergence at this pixel size and below. Time-evolving visualizations of our column density maps are available at: http://noneq.strw.leidenuniv.nl/PZF/.

In the upper panel of Fig. 2, we plot the median SMOHALOS O VI column densities in six bins between 0 and 150 kpc, with 1σ
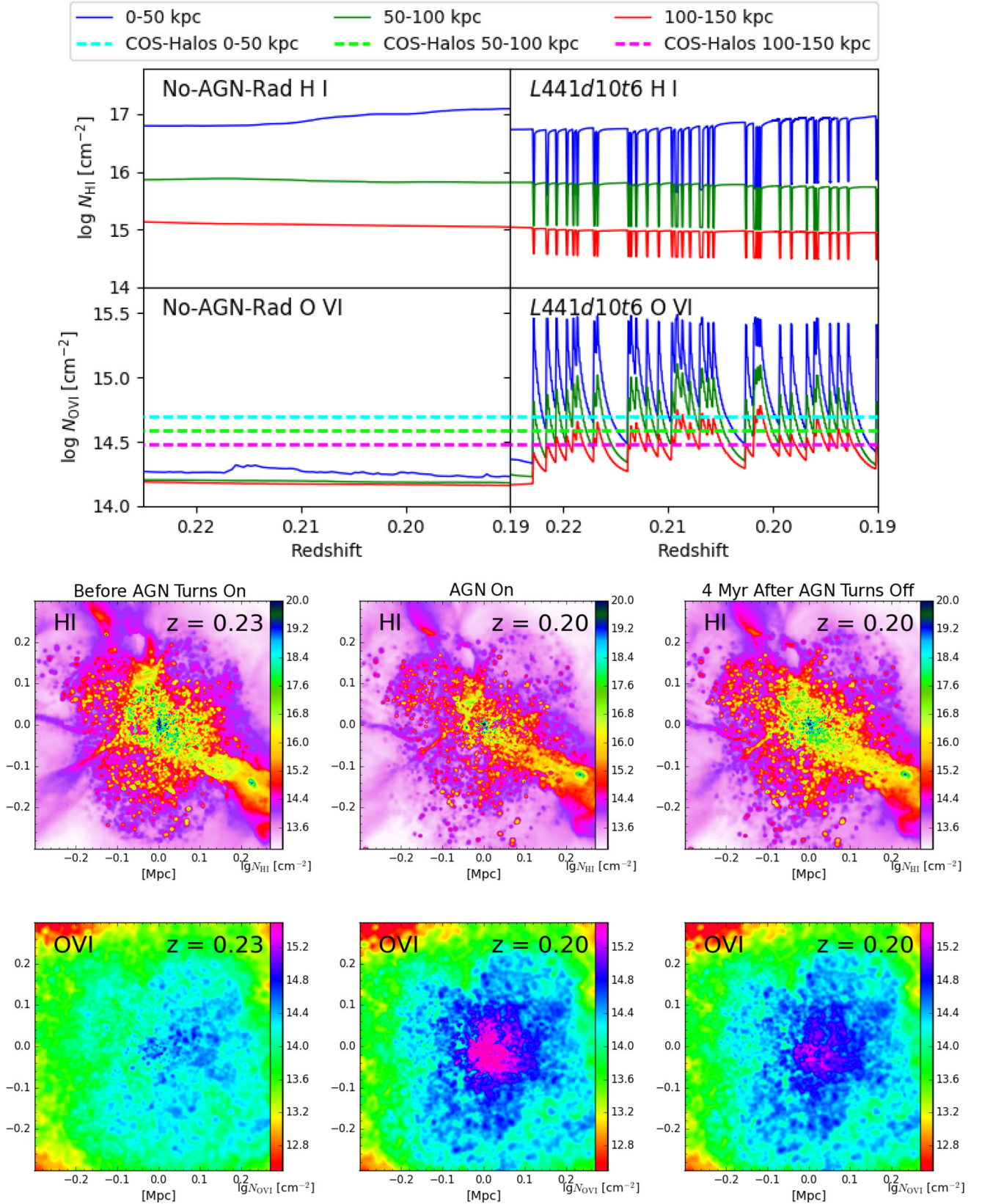
Figure 1. Upper portion: histories of median H I (upper panels) and O VI (lower panels) column densities in three impact parameter bins ($b = 0$–50, 50–100, and $100 - 150$ kpc) for the No-AGN-Rad model (left) and the reference *L441d10t6* ($L_{bol} = 10^{44.1}$ erg s^{-1}, $f_{duty} = 10$ per cent, and $t_{AGN} = 10^{6.2}$ yr) PZF model (right). COS-Halos O VI medians for the star-forming sample compiled from Werk et al. (2013) in the three impact parameter bins are shown as dashed lines for comparison; their typical $1 - \sigma$ dispersions are ≈ 0.2 dex (not shown). Lower portion: 600×600 kpc snapshots are shown for H I (upper panels) and O VI (lower panels) at three times: before the AGN turns on (left), when the AGN is on (middle), and 4 Myr after the AGN turns off (right).

Figure 2. Upper panel:mock O VI SMOHALOS realizations of the COS-Halos star-forming L^* sample comparing medians of the No-AGN-Rad model (solid grey line), the reference *L441d10t6* PZF model (dashed red line) and two other models with different AGN lifetimes $t_{AGN} = 10^{7.1}$ yr (*L441d10t7*, orange dotted) and $10^{5.0}$ yr (*L441d10t5*, green dot–dashed). One-σ dispersions are indicated by thin lines and the shaded region for each model. COS-Halos data (blue squares) are plotted for comparison. Lower panels: histograms of the SMOHALOS realizations (filled histograms) divided into two impact parameter bins (0–75 and 75–150 kpc) compared to the COS-Halos observed histograms (thick blue histogram lines). The PZF effect significantly enhances O VI column densities, and AGNs with shorter lifetimes but the same time-averaged power have greater PZF effects.

dispersions for the No-AGN-Rad model (grey) and the reference model (red). The No-AGN-Rad median is quite similar to the Opp16 SMOHALOS run for the star-forming COS-Halos galaxies, but has a smaller average 1σ dispersion (cf. 0.15 dex here, 0.3 dex in Opp16). The main difference is that the Opp16 blue sample includes five additional $M_* > 10^{10.5}$ M$_\odot$ star-forming galaxies, which have lower O VI columns in both SMOHALOS and COS-Halos. This contributes to the greater Opp16 dispersion measure, as well as using 10 galaxy zooms to simulate a wider range of M_* and SSFR in Opp16 versus using one galaxy here.

The COS-Halos O VI column densities have a dispersion of $\approx 0.15 - 0.20$ dex as well, but have much higher observed columns ($\log[N_{O VI}/\mathrm{cm}^{-2}] = 14.7$, 14.6, and 14.5 for $b = 0$–50, 50–100, and 100–150 kpc, respectively), which is $3 \times$ higher than our No-AGN-Rad model with $N_{O VI} = 10^{14.2}$ cm^{-2} inside 50 kpc and and $2 \times$ higher at beyond 100 kpc in agreement with Opp16. The reference PZF model shows an increase over the No-AGN-Rad model at all impact parameters, from 0.43 dex for $b = 0$–75 kpc to 0.25 dex for $b = 75$–150 kpc, resulting in column densities only 0.1 dex COS-Halos. Unsurprisingly, the PZF increases the $1 - \sigma$ dispersions from 0.15 to 0.25–0.4 dex.

4.1.1 Parameter variation

AGN lifetime: Fig. 2 (lower panels) also shows SMOHALOS realizations for models *L441d10t7* and *L441d10t5* corresponding to longer and shorter AGN lifetimes, respectively (but the same luminosity and duty cycle). Despite delivering the same time-averaged AGN radiation power, the PZF effect is stronger for shorter lifetimes, which pump the CGM ionization level more frequently while the recombination time-scale remains the same. OS13 and Seg17 also showed this non-linear PZF ionization effect, although if the

ionization time-scale is longer than t_{AGN}, the maximum ionization state will not be achieved. The evolution of *L441d10t7* and *L441d10t5* in Fig. 3 bear out this behaviour – O VI reaches higher columns for the $t_{AGN} = 10^{7.1}$ yr during the AGN-on phase, while $t_{AGN} = 10^{5.0}$ yr achieves lower O VI columns, but far more frequently and thereby reaching higher average $N_{O VI}$.

The SMOHALOS O VI columns during the ≈ 90 per cent of the galaxy's history with inactive AGN better match the observation for the *L441d10t5* model than for the reference *L441d10t6* model. The histograms in Fig. 2 show an excellent fit to the $b = 75$–150 kpc COS-Halos O VI distribution and overpredict the inner column densities by ≈ 0.2 dex. With over 300 AGN-on phases contributing to the time history shown in Fig. 3 for *L441d10t5* versus only four for *L441d10t7*, the 'flickering' $t_{AGN} = 10^{5.0}$ yr model has achieved a relatively steady ionization state where the O VI level has little correlation with AGN activity. This model shows that for normal expectations for SMBH parameters, O VI columns comparable to and even in excess of observed COS-Halos O VI are plausible.

AGN luminosity: $N_{O VI}$ increases with AGN luminosity, as shown in Fig. 4 using $f_{duty} = 10$ per cent and $t_{AGN} = 10^{6.2}$ yr. OS13 showed that O VI columns can decline in PZFs if the AGN is strong and the density is low because more O VI becomes ionized to O VII and above. However, the CGM is too dense and the AGN explored here are too weak to reach this limit. The best fit to the data is still the $L_{bol} = 10^{44.1}$ erg s^{-1} ($\lambda_{Edd} = 0.1$) model, and this exploration shows that low-luminosity AGNs ($L_{bol} \sim 10^{43.1}$ erg s^{-1}) are too weak to ionize O VI to the observed levels using the Sazonov et al. (2004) spectrum, at least for $f_{duty} = 10$ per cent and $t_{AGN} = 10^{6.2}$ yr. The $L_{bol} = 10^{45.1}$ erg s^{-1} model predicts too much O VI while implying a likely unsustainable s$\dot{M}_{BH} = 2.5 \times 0^{-9}$ yr^{-1} for $M_{BH} \sim 10^7$ M$_\odot$.

Duty cycle: We show the dependence of COS-Halos O VI on the duty cycle in Fig. 5 for $t_{AGN} = 10^{5.0}$ yr and $L_{bol} = 10^{44.1}$ erg s^{-1}. The PZF effect significantly declines at lower duty cycle, even though the intervals in between AGN activity average 10^7 yr for $f_{duty} = 1$ per cent, which is approximately the recombination time-scale for O VI. This contrasts to cases in OS13 where the PZF effect did not show much dependence on the duty cycle as long as the interval time was shorter than the ion recombination time. The reason for the difference here is that for the short AGN lifetimes the CGM does not reach ionization equilibrium with the enhanced AGN+EGB field. In the limit of short AGN lifetimes, Seg17 demonstrated the PZF approaches a quasi-steady-state ionization level described by the time-averaged AGN+EGB field. Here, we see the effect of the flickering AGN with higher duty cycles, and therefore higher time-averaged power, reaching higher ionization levels.

Time-averaged SMBH growth rate kept constant: The final parameter variation we explore in isotropic models is leaving s$\dot{M}_{BH}$ constant at 8×10^{-11} yr^{-1} but varying f_{duty} and L_{bol} as we show in Fig. 6 for $t_{AGN} = 10^{5.0}$ yr. Our hypothesis is that there may exist a combination of duty cycle and AGN luminosity that maximizes the PZF effect while keeping the SMBH growth rate similar to the sSFR ($\approx 10^{-10}$ yr^{-1}). Despite a factor of 32 difference in AGN luminosity and duty cycle explored, there is surprisingly little difference in the PZF effect, especially for the $t_{AGN} = 10^{5.0}$ yr lifetime. Models with $t_{AGN} = 10^{6.2}$ yr appear in Table 2 and show the high duty cycle fraction, $f_{duty} = 32$ per cent model having slightly higher inner O VI column densities, but otherwise very little difference. Higher f_{duty} values are disfavoured, since more galaxies would appear as AGN.

The exploration here shows that the PZF effect does not depend strongly on how the AGN radiative power is distributed in
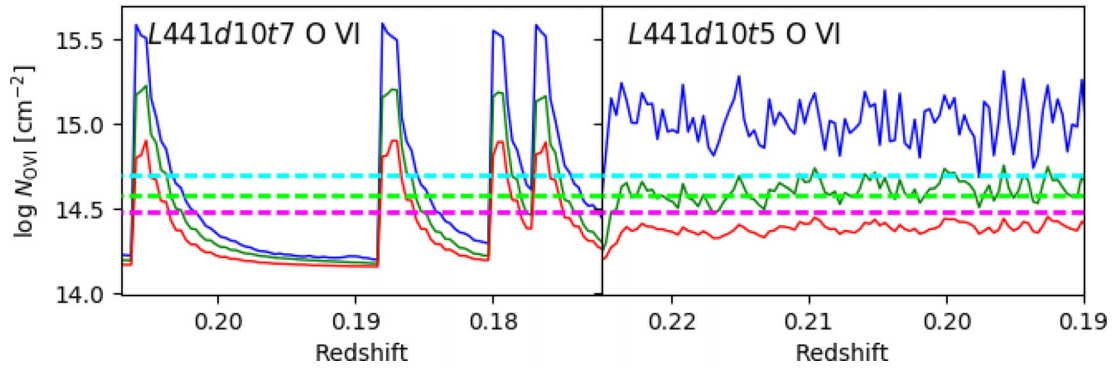
Figure 3. O VI time histories are displayed for the *L441d10t7* ($t_{AGN} = 10^{7.1}$ yr, left) and *L441d10t5* ($t_{AGN} = 10^{5.0}$ yr, right) models as in Fig. 1. The same time-averaged power results in very different O VI column densities with the left-hand panel showing four distinct AGN-on episodes and the right-hand panel achieving a near steady ionization state with over 300 AGN-on episodes.
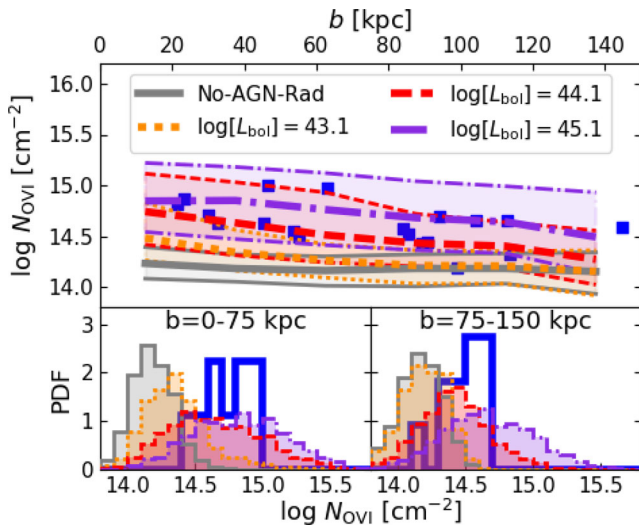

Figure 4. The dependence of O VI column density profiles on AGN luminosity for the SMOHALOS realizations are plotted as in Fig. 2. O VI column densities increase for stronger AGN, because more CGM oxygen in lower ions is ionized up to O VI. The Eddington limited $L_{bol} = 10^{45.1}\,\mathrm{erg\,s^{-1}}$ AGN creates too much O VI with too large of a dispersion compared to COS-Halos in the lower panels, while the $L_{bol} = 10^{43.1}\,\mathrm{erg\,s^{-1}}$ AGN is too weak.

time for $s\dot{M}_{BH} = 8 \times 10^{-11}$ yr^{-1}, which corresponds to a time-averaged AGN luminosity of $\langle L_{bol} \rangle = 10^{42.6}$ erg s^{-1}. Fig. 10 of Seg17 explicitly demonstrates this effect. In the limit of AGN interval times $\ll t_{rec}$, the column densities approach the steady state of constant ionization by the time averaged AGN+EGB field.

Interestingly, the *L446d01t5*, which is plotted in Fig. 6 in dotted pink, is a new model[2] that matches the averaged properties of an AGN occupying $M_* = 10^{10}$–$10^{10.5}$ M$_\odot$ star-forming galaxies according to Aird et al. (2017). Although they derive distributions of λ_{Edd} as a function of galaxy redshift, mass, and type (star-forming versus quiescent), their fig. 6 gives the mean duty cycle fraction above $\lambda_{Edd} > 0.01$ (1 per cent) and their fig. 8 gives the average Eddington ratio above $\lambda_{Edd} > 0.01$ ($\lambda_{Edd} \sim 0.1$). The $L_{bol} = 10^{44.6}\,\mathrm{erg\,s^{-1}}$ luminosity implies $\lambda_{Edd} = 0.3$ for our assumed $M_{BH} = 10^{7.0}$ M$_\odot$, but because Aird et al. (2017) base their SMBH masses using $M_{BH} = 0.002M_*$, their model implies

---

[2] Added in the revision as a suggestion from the referee.

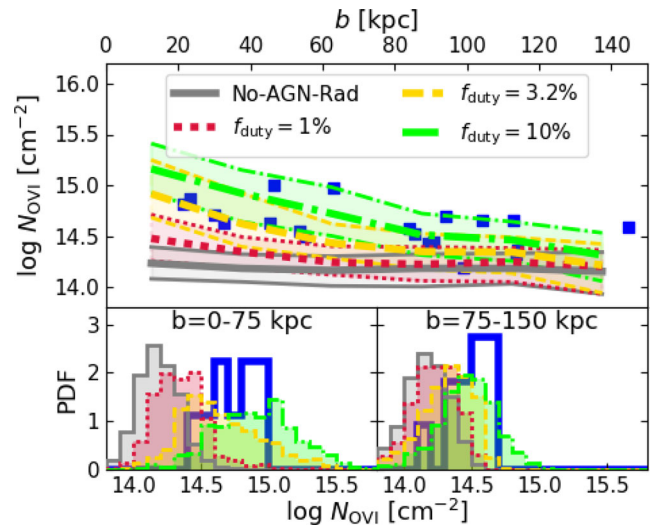**Figure 5.** The dependence of O VI column density profiles on duty cycle fraction for the SMOHALOS realizations are plotted as in Fig. 2. Using $t_{AGN} = 10^5$ yr and $L_{bol} = 10^{44.1}\,\mathrm{erg\,s^{-1}}$, the O VI columns decrease for lower duty cycles, owing to declining AGN time-averaged power.

$M_{BH} \approx 10^{7.5}$ M$_\odot$. Nevertheless, this demonstrates a significant PZF effect using the population characteristics from a recent X-ray-selected survey assuming a randomly flickering SMBH with average interval times between AGN episodes of $\approx 10^7$ yr.

4.2 Anisotropic models

Thus far we have explored isotropically emitting models, even though optically thick dust tori are expected to surround the central SMBH engine during accretion episodes. Here, we explore a simple anisotropic AGN model by assuming a biconical opening angle of $120°$ corresponding to a covering factor of 2π steradians. We set the axis of the bicone using the angular momentum vector of star-forming gas within $3h^{-1}$kpc at that timestep, which serves as a proxy for shielding by dust in the torus and/or extended dust in the galactic disc. No AGN radiation leaks in the equatorial direction corresponding to the other 2π steradians, which is an assumption that may underestimate the PZF effect if the dust torus is not Compton thick, as we discuss in Section 5. We also run a *L441d10t6-bicone* model with the bicone aligned to the stellar disc within $10h^{-1}$kpc, and find that the cone axis varied less, but there
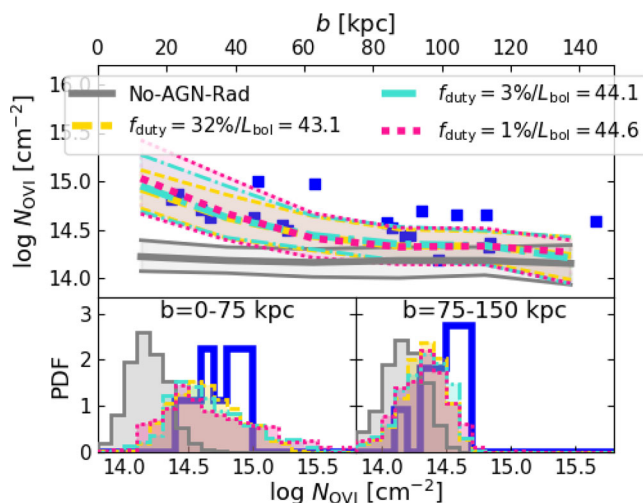
Figure 6. SMOHALOS realizations are plotted as in Fig. 2 using $t_{AGN} = 10^5$ yr, but keeping $s\dot{M}_{BH} = 8 \times 10^{-11}$ yr^{-1} through a combination of varying duty cycle and AGN luminosity. There is little dependence on how AGN radiation is distributed in time given this AGN average power. The $f_{duty} = 10$ per cent $L_{bol} = 10^{43.6}$ erg s^{-1} model (*L436d10t5*, not shown) shows identical statistics to the other PZF models shown here.
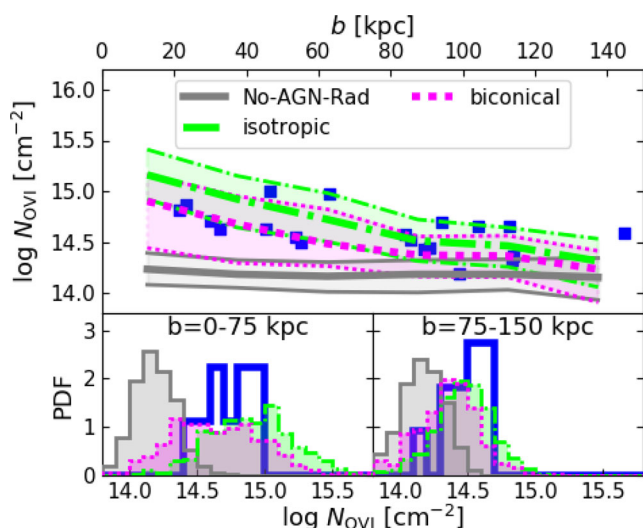

Figure 7. SMOHALOS realizations are plotted as in Fig. 2 using $t_{AGN} = 10^5$ yr models, but showing the effect of using a biconical opening angle (*L441d10t5-bicone*) compared to the isotropic model (*L441d10t5*). The AGN radiative power is half as strong in the latter, but still creates a significant PZF effect.

is hardly any difference in the O VI statistics. We also allow our bicone to have random orientations, which applies the assumption that the black hole accretion disc is randomly oriented with respect to the galactic disc and is responsible for obscuration and find no difference in the O VI statistics.

The SMOHALOS results are shown in Fig. 7, showing that the O VI column densities are intermediate between the No-AGN-Rad model and the isotropic cases. While this is not surprising, the biconical O VI median column density is stronger than halfway between the No-AGN-Rad and isotropic cases even though half the CGM volume is ionized with a 120° opening angle. This is particularly apparent for the $t_{AGN} = 10^{5.0}$ yr biconical model (*L441d10t5-bicone*, magenta dotted line). Part of the reason for this behaviour is that more than half of the sight lines are enhanced due to the galaxy LOS

geometry – even if only half the volume is ionized, more than half the sight lines intersect the ionization cone, even for a 90° inclined torus. We compile statistics in the *x*, *y*, and *z* projections regardless of torus orientation, because the torus orientation changes and the three projection axes should average out.

If the dust obscuration primarily arises from the BH accretion disc that is decoupled from the galactic disc orientation, then a model with random orientation for each AGN episode is more appropriate. We therefore run a *L441d10t5-bicone* model (not shown), where the bicone axis orientation is randomly oriented, which yields identical medians and dispersions as the gas-aligned bicone case. Our AGN bicone axis orientation does not appear to affect the statistics of a COS-Halos-like survey. Short AGN lifetimes again achieve a quasi-steady-state ionization level with the AGN+EGB field, where the AGN field is half as strong as in the isotropic case.

The *L441d10t5-bicone* model provides a very good fit to the COS-Halos data. Some of this model's column densities at larger *b* are slightly low compared to COS-Halos, but all the highest data points are within the $2 - \sigma$ range (not shown). It is not worthwhile to tweak the model to get a better match. We can certainly find a better matching model with a slightly larger opening angle, a slightly larger duty cycle or AGN luminosity, a shorter AGN lifetime, or some other combination of all of these. However, we have shown that this approximate model, which grows its SMBH at an evolutionarily sustainable rate, satisfies the COS-Halos O VI statistics. For consistency with other SMOHALOS models that apply statistics only to phases when the AGN is off and the galaxy appears to be a normal star-forming galaxy, we should include snapshot frames with active but obscured AGN. However, we do not do so because this makes only a small difference. More importantly, this means that 5 per cent, instead of 10 per cent of star-forming galaxies, will be observed as active AGN in the optical, better reconciling the non-AGN COS-Halos detections on the BPT diagram (Werk et al. 2012).

4.3 Other ions

Other metal ions should be affected by PZFs, including C IV, which, as Seg17 shows, can both be enhanced and reduced. We consider low and intermediate ions commonly observed around COS-Halos galaxies (Si II, Si III, Si IV), as well as N V for our favoured *L441d10t5-bicone* model in Fig. 8. The lower the ionization potential, the higher the physical density traced (e.g. Ford et al. 2013), and therefore the shorter the typical recombination time. Low ions column densities are primarily reduced in PZFs, while N V, another high ion, is enhanced. The intermediate ion Si IV is at the threshold where it is neither reduced nor enhanced significantly. The Si II and Si III medians are reduced by 0.1–0.2 dex, but the larger effect is an increased dispersion at low column densities for these species.

Oppenheimer et al. (2017) compare SMOHALOS low-ion COS-Halos measurements without considering PZFs, finding relatively good agreement for Si species, although they note that Si III is 2–3 × too strong, which PZFs appear to help reduce. That work also finds good agreement between simulated and observed Si II. However, this ion is also sensitive to self-shielding, which enhances Si II column densities by a factor of ≈2 over the standard uniform Haardt & Madau (2001) EGB model. Combining PZFs with self-shielding in simulations will assist the assessment of how these two effects combine to alter low-ion column densities.

N V is strongly enhanced, similar to O VI, and appears to be consistent with most COS-Halos observations. Werk et al. (2016) explored the N V/O VI ratios in COS-Halos, showing most models indicate tension with the low N V columns observationally ascertained mainly using upper limit non-detections (plotted in the lower
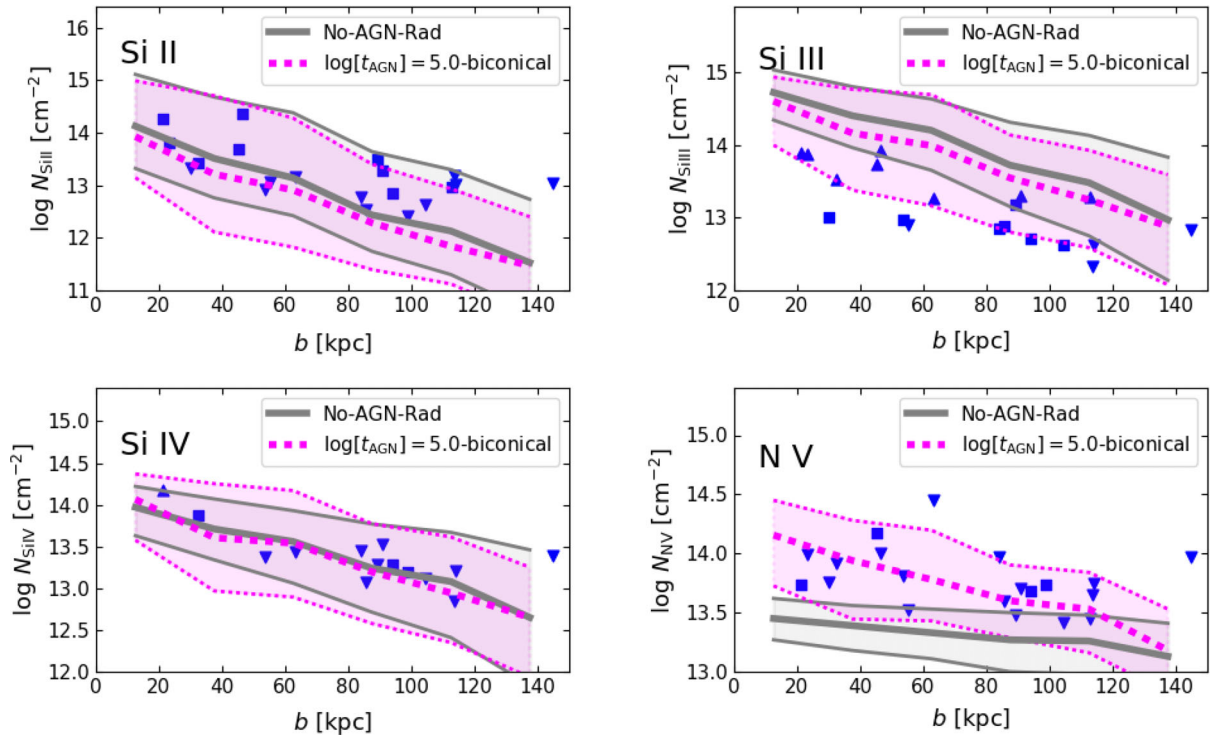
Figure 8. Other ions are displayed for the *L441d10t5-bicone* model (dotted magenta) relative to the No-AGN-Rad model (solid grey), including Si II (upper left), Si III (upper right), Si IV (lower left), and N V (lower right). Medians (thick lines) and 1σ dispersion (thin lines) are displayed. Blue squares indicate detections, upside-down triangles are upper limits for non-detections, and right-side-up triangles are lower limits for saturated lines. Low ions (Si II, Si III) are moderately reduced by the PZF effect, high ions (O VI, N V, C IV) are increased, and an intermediate ion like Si IV remain relatively unchanged.

right-hand panel of Fig. 8). The PZF effect here does not appear to alter N V/O VI ratios for our one halo. We do not show C IV since it is not observed by COS-Halos, but this ion is enhanced by $\approx$0.2 dex over the inner 125 kpc as expected for an ion intermediate between Si IV and N V, as also shown by Seg17.

Finally, we display idealized mock spectra in Fig. 9 at six impact parameters between 25 and 150 kpc. SpecWizard, described in Theuns et al. (1998) and Schaye et al. (2003), is used to generate idealized, noiseless spectra without instrumental broadening. The No-AGN-Rad model (left) is compared to the *L441d10t5-bicone* when the AGN is off (right) for three species (O VI-green, Si III-red, and H I-black) in representative LOSs at $z = 0.204$. The same LOSs are used in the two models from the same snapshot output, and while the two models correspond to separate simulation runs since $z = 0.235$ resulting in slightly different gas distributions, the same absorption line structures can be seen in almost every LOS as best exemplified by H I at 50–150 kpc. As expected, O VI is enhanced, especially at $b < 100$ kpc, showing shallower smooth components in the No-AGN-Rad model and narrower components in the PZF model. Si III shows individual narrow component substructure in both cases, which is slightly reduced in the PZF model. Total integrated column densities listed in each subpanel can be compared across the runs, and the column densities are typical compared to the column density ranges in Figs 7 (O VI) and 8 (Si III).

Werk et al. (2016) explored the component substructure using a similar plot (their fig. 5) and defined O VI components relative to their alignment with lower metal ions, represented here by Si III. They find that about 80 per cent of O VI absorbers are well-aligned with low ions, with half being broad O VI absorbers (*b*-parameter >40 km s^{-1}) and half being narrow O VI absorbers (<40 km s^{-1}). The aligned Si III lines are mostly narrow. Our mock PZF spectra

show many more aligned O VI-Si III absorbers than the No-AGN-Rad model, especially for narrower O VI components (e.g. -100 and 0 km s^{-1} at 25 kpc, -130 and -100 km s^{-1} at 50 kpc, 30 km s^{-1} at 150 kpc). This is an encouraging finding, given the Werk et al. (2016) results, but a direct comparison between mock spectra and COS-Halos, where instrumental broadening from the COS line spread function blends together components and noise is included, is beyond the scope of this work. OS13 argued that PZF models can create aligned low and high metal ion component absorbers as observed (e.g. Tripp et al. 2011) that are not possible with equilibrium models. A key result is that our narrower O VI components are related to the PZF while broader components in the No-AGN-Rad model are related to the collisionally ionized O VI (Opp16). The latter still exist in our PZF models, but the PZF adds narrow O VI mainly at smaller impact parameters. Future work will further analyse mock spectra and compare to the aligned absorber component categories introduced by Werk et al. (2016).

5 DISCUSSION

OS13 explored how flickering low-z Seyfert galaxies might ionize their local CGM, arguing that O VI column densities could be significantly enhanced by photoionization. Since that publication, two main findings about AGN have strengthened the case for PZFs existing around normal star-forming galaxies: (1) shorter AGN lifetimes (Section 3.2) and (2) SMBH growth rates similar to, or in excess of, the stellar mass growth rate (Section 3.3). Our main result is that if a star-forming disc galaxy grows its SMBH at the cosmologically expected rate and had luminous AGN activity within the previous 10–20 Myr, then its CGM is highly likely to show enhanced O VI due to the PZF effect.
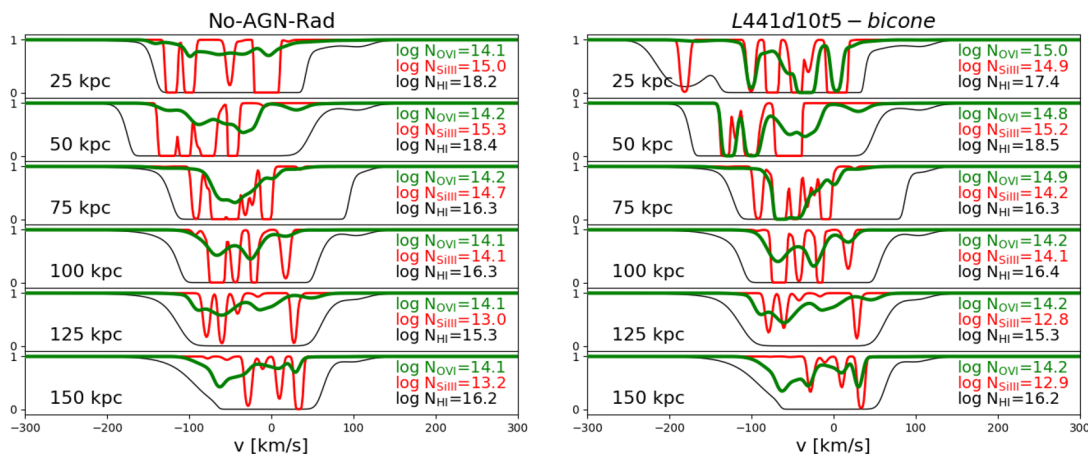
Figure 9. Mock spectra generated using SpecWizard under idealized conditions (no noise or instrumental broadening added). Six LOS spanning $b = 25$–$150\,\mathrm{kpc}$ show O VI (thick green), Si III (red), and H I (thin black) for the same sight lines in two $z = 0.204$ snapshots (No-AGN-Rad on left, & *L441d10t5-bicone* PZF on right). Total column densities integrated using SpecWizard are listed in each panel showing PZF increases in O VI, slight decreases in Si III, and similar structures in H I. Note that these are two different simulation runs, which can lead to random differences that are not directly caused by the radiation field.

Our exploration here represents a proof of concept that the highly ionized CGM might be driven far out of ionization equilibrium by AGN radiation in the low-redshift Universe. More sophisticated, follow-up modelling needs to consider physically derived SMBH accretion histories (e.g. Novak et al. 2011; Gabor & Bournaud 2013), radiative transfer with light travel effects, as well as the NEQ ionization from a fluctuating field introduced here. We expect light travel time effects (included in Seg17) to be important when considering how the CGM ionization level correlates with the AGN activity. The light travel time is $\approx 5 \times 10^5$ yr out to 150 kpc, which is significant compared to plausible AGN lifetimes. The case of the flickering AGN with $t_{\mathrm{AGN}} \sim 10^5$ yr and $f_{\mathrm{duty}} \sim 10$ per cent results in ionization that decorrelates from AGN activity, and achieves what can be described as a PZF steady state.

Our obscured torus bicone model is simplistic, intended only to explore the possibility of anisotropic AGN emission, which is especially likely in low-luminosity AGN residing in disc galaxies with significant dust. Anisotropic models open the possibility of PZFs arising and being enhanced due to dust obscuration that can change on a short time-scale, especially if the dust is associated with the SMBH engine where its orbital time may be shorter than the AGN lifetime. It is also unlikely that these AGNs are Compton thick, meaning that that X-ray radiation will escape, and how such a spectrum ionizes the CGM is beyond the scope of this paper. Another crude approximation is the binary nature of our AGN (either on or off), when in reality the AGN emission spectrum escaping into the CGM depends on the amount and type of obscuration. Finally, we do not discount the possibility of extreme UV or soft X-ray radiation from star formation escaping the galaxy and ionizing O VI (e.g. Cantalupo 2010; Vasiliev, Ryabova & Shchekinov 2015), possibly anisotropically along the semiminor axis of the galaxy.

The *L441d10t5-bicone* model represents our favoured model because (1) it agrees with the s$\dot{M}_{\mathrm{BH}}$ of an SMBH in a star-forming disc, (2) the 10 per cent duty cycle (observed to be 5 per cent with obscuration) is statistically reconcilable with observing no AGN in COS-Halos, (3) it appeals to the shorter AGN lifetimes supported by recent work (Gabor & Bournaud 2013; Schawinski et al. 2015), and (4) its biconical ionization considers obscuration by a dust torus and/or dust in the star-forming disc. If the dust obscuration is aligned with the stellar disc, then this could help explain

why Kacprzak et al. (2015) observes that the azimuthal dependence of O VI around bluer galaxies peaks along the semiminor axis. This study partially motivated our consideration of the bicone model, since Kacprzak et al. (2015) suggest a wide opening angle of stronger O VI at $b \lesssim 100\,\mathrm{kpc}$. Our model provides an alternative to the model of star formation-driven winds being responsible for strong O VI along the semiminor axis and represents an addendum to the Opp16 model of O VI 'haloes' tracing the virialized 3×10^5 K gas of L^* galaxies with little relation to recent star formation.

Passive galaxies: We do not explore the passive red COS-Halos sample here, but the PZF effect could also enhance the circumgalactic O VI columns for these galaxies. Opp16 showed that while the standard EAGLE zooms were consistent with most of the O VI upper limits, 3 of the 12 COS-Halos passive galaxies showed $N_{\mathrm{O\,VI}} = 10^{14.2}$–$10^{14.4}$ cm^{-2} that were not reproduced in the Opp16 SMOHALOS realizations. There may be reason to believe the PZF effect is not as common around these galaxies, because passive galaxies are much less likely to be accreting the cold gas that feeds AGN activity as well as star formation. While one may expect less low ionization cold gas in a passive galaxy's CGM, Werk et al. (2013) showed that low and intermediate ions are nearly as common around passive galaxies as around star-forming galaxies. The predicted Opp16 O VI column densities for passive galaxies are low enough ($N_{\mathrm{O\,VI}} \sim 10^{13-13.5}$ cm^{-2}) that the PZF effect could raise their values and still be consistent with the COS-Halos measurements.

Collisionally ionized O VI: Opp16 argued that COS-Halos O VI is collisionally ionized tracing $T \sim 10^{5.5}$ K virialized gas in and around L^* haloes hosting normal star-forming galaxies, but they did not consider radiation from flickering AGN. In Fig. 10, we plot the oxygen mass and ion fractions as a function of radius from the galaxy for the *M5.3* No-AGN-Rad (left) and a typical output for the *L441d10t5* PZF model (right) at $z = 0.19$ with the AGN off for approximately 0.5 Myr. The lower panels show the O VI component divided into collisionally ionized and photoionized components using a cut of $T = 10^5$ K. The O VI collisionally ionized component, mainly between 1and2R_{200} (200–500 kpc; Opp16), remains for the PZF, but the PZF has an additional photoionized O VI component,
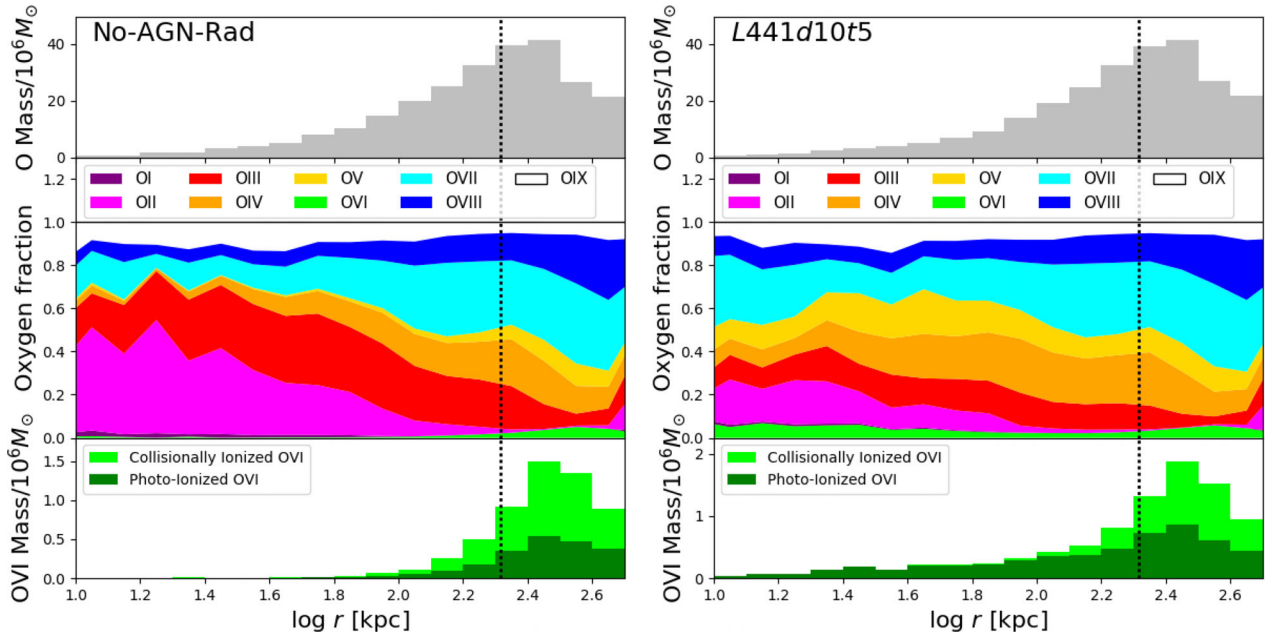
Figure 10. The oxygen mass budgets and ionization fractions at $z = 0.19$ plotted as functions of galactocentric radius for the No-AGN-Rad model (left) and the *L441d10t5* model (right). The upper panels show oxygen mass, which is essentially identical in the two cases. The centre panels indicate the oxygen ionization fractions and the lower panels show the O VI mass divided into collisionally ionized and photoionized components. The dotted vertical line indicates the virial radius. AGN photoionize O VI mainly inside R_{200}, while O VI remains collisionally ionized mainly outside R_{200}. Note that radii $\gtrsim R_{200}$ will often be projected on to impact parameter $<R_{200}$.

mainly inside R_{200}, that leads to stronger O VI. Mock spectra in Fig. 9 show narrow components due to the PZF added to broader components from collisional ionization. The overall circumgalactic O VI ionization fraction of gas within 500 kpc is ≈2 per cent in the No-AGN-Rad model (in agreement with Opp16), while this fraction increases to ≈3–3.5 per cent for the *L441d10t5* PZF. The Opp16 model where O VI traces the virial temperatures of star-forming haloes still applies, but the PZF effect adds a comparable amount of photoionized O VI within the virial radius.

IGM O VI statistics: As mentioned at the beginning of Section 2, Rahmati et al. (2016) showed an underestimate of the frequency of $N_{\mathrm{O\,VI}} > 10^{14.5}\,\mathrm{cm}^{-2}$ absorbers at $z \approx 0$–0.5 in their fig. 2. However, this result used the lower resolution Ref-L100N1504 EAGLE volume, and we use the Recal-L025N0752 EAGLE resolution and prescription for our *M5.3* zooms. Opp16 demonstrated that O VI results are statistically identical between the *M5.3* NEQ zooms (i.e. the No-AGN-Rad model) and the Recal-L025N0752 volume. Rahmati et al. (2016) tested resolution convergence, finding $3 \times$ more $N_{\mathrm{O\,VI}} = 10^{14.5}\,\mathrm{cm}^{-2}$ absorbers in the Recal-L025N0752 volume (their fig. B2), which better agrees with the observations compiled in their fig. 2. Opp16 showed that the *M5.3* zooms produced O VI columns 0.26 dex higher in the L^* CGM than the lower resolution EAGLE volumes and argued that this also supported better agreement with high-column O VI IGM statistics. PZFs around L^* galaxies should raise the frequency of high-column O VI absorbers even more, but their frequency in an IGM O VI survey like Danforth et al. (2016) is low. In summary, PZFs are unlikely to contribute much to the observed O VI IGM statistics, and the level of agreement between the Rahmati et al. (2016) Recal-L025N0752 volume results and the IGM O VI observations remain approximately the same.

Spectral hardness of AGN spectrum: We assume the Sazonov et al. (2004) spectrum, which uses an extreme-UV (EUV) slope

of $\nu^{-1.7}$ below 1216 Å, which is slightly harder than the assumed Haardt & Madau (2001) EGB. This spectrum was derived for the average Type I unobscured quasar from a variety of observations available at that time. More recent works by Stevans et al. (2014) found an EUV slope of $\nu^{-1.41}$, which is even harder and would create an even greater PZF effect for high ions like O VI as discussed in OS13. Observing the EUV slope of Seyfert-like galaxies is critical for understanding the magnitude of the PZF effect around star-forming galaxies, but we note that our assumption of the Sazonov et al. (2004) spectrum could be a conservative assumption for the PZF effect.

6 SUMMARY

AGN PZFs ionizing their CGM were introduced by Oppenheimer & Schaye (2013b), initially as a test of NEQ ionization and cooling in the presence of rapidly changing radiation fields. Seg17 ran the first cosmological hydrosimulations of PZFs using individual EAGLE haloes, finding high ions are significantly enhanced for a variety of parameters. Here, we argue that PZFs significantly enhance O VI observed by COS-Halos around normal star-forming galaxies (Tumlinson et al. 2011) using the first dynamic simulations including PZFs. AGNs ionize the metal-enriched CGM around typical star-forming disc galaxies and then turn off leaving CGM metal ions far out of equilibrium for time scales longer than the time between subsequent AGN episodes. The central requirement for a significant PZF effect is therefore that the star-forming galaxy hosted an active AGN within a time-scale comparable to the recombination time of a high metal ion, which for circumgalactic O VI is of the order of 10^7 yr.

We vary AGN lifetimes, luminosities, duty cycle fractions, and isotropy in an EAGLE zoom simulation of a typical star-forming galaxy using the NEQ module introduced in Opp16 with the ad-

dition of a spatially and time variable AGN field.[3] Our focus is to investigate whether an AGN can reproduce the strong O VI around star-forming galaxies observed by COS-Halos while having an evolutionarily sustainable SMBH growth rate and a small duty cycle fraction so that most galaxies appear as inactive AGN. We find that models with AGN bolometric luminosities $\gtrsim 10^{43.6}\,\mathrm{erg\,s^{-1}}$, duty cycle fractions $\lesssim 10\,\mathrm{per\,cent}$, and a time-averaged power $\langle L_{\mathrm{bol}} \rangle \gtrsim 10^{42.6}\,\mathrm{erg\,s^{-1}}$ satisfy these requirements. Critically, H I does not show the PZF effect because high ionization fraction enables it to quickly return to equilibrium with the extragalactic background, resulting in strong H I column densities as observed around COS-Halos (Thom et al. 2012). Our favoured models have specific SMBH accretion rates $\approx 2 \times$ higher than the specific SFR of a typical star-forming galaxy, which is consistent with cosmologically expected growth rates of typical low-mass SMBHs occupying disc galaxies with $M_* \sim 10^{10}$–$10^{10.5}\,\mathrm{M_\odot}$. Interestingly, recent surveys of low-redshift, star-forming galaxies of this mass (Aird et al. 2017) find X-ray-selected AGN with luminosities, duty cycle fractions, and time-averaged powers fitting our requirements for significant PZF effects.

AGN lifetimes are more difficult to constrain observationally, but recent evidence of flickering AGN with time scales of 10^5 yr or less around star-forming galaxies in the evolved Universe (Sections 3 and 5) supports our argument for NEQ PZFs in the low-redshift CGM. Models with $t_{\mathrm{AGN}} \lesssim 10^6$ yr can enhance O VI columns by the factors of 2–3 necessary to match COS-Halos. Time scales $\lesssim 10^5$ yr result in the CGM ionization becoming temporally decorrelated from AGN activity, resulting in a quasi-steady-state PZF with the ionization level described by the time-averaged AGN+EGB field (Seg17). Additionally, we show in Section 4.3 that such models can create narrow O VI absorbers that are well aligned with low and intermediate ions as observed by Werk et al. (2016). The dynamics of the CGM gas appear unaltered between the model with no AGN radiation (No-AGN-Rad) and the AGN PZF runs, which agrees with Seg17 that AGN photoheating does not significantly alter cooling in the CGM.

We argue that PZFs are a necessary consideration when deriving and interpreting physical conditions of the highly ionized CGM probed by the Cosmic Origins Spectrograph. Our model presents a plausible solution for the underestimates of O VI column densities reported by several teams analysing the range of cosmological hydrodynamic simulations of galaxy formation and evolution. If normal disc galaxies in the evolved Universe grow their SMBH at the cosmologically expected rate, the PZF effect is likely to affect observations of the metal-enriched CGM.

ACKNOWLEDGEMENTS

REFERENCES

Aird J., Coil A. L., Georgakakis A., 2017, MNRAS, 465, 3390
Bahé Y. M. et al., 2016, MNRAS, 456, 1115
Baldwin J. A., Phillips M. M., Terlevich R., 1981, PASP, 93, 5
Bland-Hawthorn J., Maloney P. R., Sutherland R. S., Madsen G. J., 2013, ApJ, 778, 58
Borisova E., Lilly S. J., Cantalupo S., Prochaska J. X., Rakic O., Worseck G., 2016, ApJ, 830, 120
Bower R., Schaye J., Frenk C. S., Theuns T., Schaller M., Crain R. A., McAlpine S., 2017, MNRAS, 465, 32
Cantalupo S., 2010, MNRAS, 403, L16
Chabrier G., 2003, PASP, 115, 763
Crain R. A. et al., 2015, MNRAS, 450, 1937
Crain R. A. et al., 2017, MNRAS, 464, 4204
Danforth C. W. et al., 2016, ApJ, 817, 111
Ford A. B., Oppenheimer B. D., Davé R., Katz N., Kollmeier J. A., Weinberg D. H., 2013, MNRAS, 432, 89
Ford A. B. et al., 2016, MNRAS, 459, 1745
Furlong M. et al., 2015, MNRAS, 450, 4486
Gabor J. M., Bournaud F., 2013, MNRAS, 434, 606
Gnat O., Ferland G., 2012, ApJS, 199, 20
Gonçalves T. S., Steidel C. C., Pettini M., 2008, ApJ, 676, 816
Gutcke T. A., Stinson G. S., Macciò A. V., Wang L., Dutton A. A., 2017, MNRAS, 464, 2796
Haardt F., Madau P., 2001, in Neumann D. M., Van J. T. T., eds, Clusters of galaxies and the high redshift universe observed in X-rays, Recent results of XMM-Newton and Chandra, XXXVIth Rencontres de Moriond, XXIst Moriond Astrophysics Meeting, Savoie, France
Haggard D., Green P. J., Anderson S. F., Constantin A., Aldcroft T. L., Kim D.-W., Barkhouse W. A., 2010, ApJ, 723, 1447
Haiman Z., Hui L., 2001, ApJ, 547, 27
Häring N., Rix H.-W., 2004, ApJ, 604, L89
Hickox R. C., Mullaney J. R., Alexander D. M., Chen C.-T. J., Civano F. M., Goulding A. D., Hainline K. N., 2014, ApJ, 782, 9
Hopkins P. F., Hernquist L., 2006, ApJS, 166, 1
Hopkins P. F., Hernquist L., Cox T. J., Di Matteo T., Robertson B., Springel V., 2006, ApJS, 163, 1
Hopkins P. F., Hernquist L., 2009, ApJ, 698, 1550
Hummels C. B., Bryan G. L., Smith B. D., Turk M. J., 2013, MNRAS, 430, 1548
Jakobsen P., Jansen R. A., Wagner S., Reimers D., 2003, A&A, 397, 891
Jenkins A., 2010, MNRAS, 403, 1859
Jenkins A., Booth S., 2013, preprint (arXiv:1306.5771)
Jones M. L., Hickox R. C., Black C. S., Hainline K. N., DiPompeo M. A., Goulding A. D., 2016, ApJ, 826, 12
Kacprzak G. G., Muzahid S., Churchill C. W., Nielsen N. M., Charlton J. C., 2015, ApJ, 815, 22
King A., Nixon C., 2015, MNRAS, 453, L46
Kollmeier J. A. et al., 2006, ApJ, 648, 128
Lagos C. d. P. et al., 2015, MNRAS, 452, 3815
Lintott C. J. et al., 2009, MNRAS, 399, 129

---

[3] Please visit http://noneq.strw.leidenuniv.nl/PZF/ for visualizations of the PZF effect.

Martini P., Weinberg D. H., 2001, ApJ, 547, 12

McAlpine S., Bower R. G., Harrison C. M., Crain R. A., Schaller M., Schaye J., Theuns T., 2017, MNRAS, 468, 3395

Novak G. S., Ostriker J. P., Ciotti L., 2011, ApJ, 737, 26

Oppenheimer B. D., Schaye J., 2013a, MNRAS, 434, 1043

Oppenheimer B. D., Schaye J., 2013b, MNRAS, 434, 1063 (OS13)

Oppenheimer B. D. et al., 2016, MNRAS, 460, 2157 (Opp16)

Oppenheimer B. D., Schaye J., Crain R. A., Werk J. K., Richings A. J., 2017, MNRAS, preprint (arXiv:1709.07577)

Peeples M. S., Werk J. K., Tumlinson J., Oppenheimer B. D., Prochaska J. X., Katz N., Weinberg D. H., 2014, ApJ, 786, 54

Planck Collaboration I, 2014, A&A, 571, A1

Rahmati A., Schaye J., Bower R. G., Crain R. A., Furlong M., Schaller M., Theuns T., 2015, MNRAS, 452, 2034

Rahmati A., Schaye J., Crain R. A., Oppenheimer B. D., Schaller M., Theuns T., 2016, MNRAS, 459, 310

Richings A. J., Schaye J., Oppenheimer B. D., 2014, MNRAS, 440, 3349

Rosas-Guevara Y. M. et al., 2015, MNRAS, 454, 1038

Rosas-Guevara Y., Bower R. G., Schaye J., McAlpine S., Dalla Vecchia C., Frenk C. S., Schaller M., Theuns T., 2016, MNRAS, 462, 190

Salpeter E. E., 1964, ApJ, 140, 796

Satyapal S., Secrest N. J., McAlpine W., Ellison S. L., Fischer J., Rosenberg J. L., 2014, ApJ, 784, 113

Sazonov S. Y., Ostriker J. P., Sunyaev R. A., 2004, MNRAS, 347, 144

Schawinski K., Koss M., Berney S., Sartori L. F., 2015, MNRAS, 451, 2517

Schaye J., Aguirre A., Kim T.-S., Theuns T., Rauch M., Sargent W. L. W., 2003, ApJ, 596, 768

Schaye J. et al., 2015, MNRAS, 446, 521 (Sch15)

Schirber M., Miralda-Escudé J., McDonald P., 2004, ApJ, 610, 105

Schirmer M. et al., 2016, MNRAS, 463, 1554

Scott J., Bechtold J., Dobrzycki A., Kulkarni V. P., 2000, ApJS, 130, 67

Segers M. C., Crain R. A., Schaye J., Bower R. G., Furlong M., Schaller M., Theuns T., 2016, MNRAS, 456, 1235

Segers M. C., Oppenheimer B. D., Schaye J., Richings A. J., 2017, MNRAS, 471, 1026 (Seg17)

Shen Y., Greene J. E., Strauss M. A., Richards G. T., Schneider D. P., 2008, ApJ, 680, 169

Springel V., 2005, MNRAS, 364, 1105

Stevans M. L., Shull J. M., Danforth C. W., Tilton E. M., 2014, ApJ, 794, 75

Sun M. et al., 2015, ApJ, 802, 14

Suresh J., Rubin K. H. R., Kannan R., Werk J. K., Hernquist L., Vogelsberger M., 2017, MNRAS, 465, 2966

Theuns T., Leonard A., Efstathiou G., Pearce F. R., Thomas P. A., 1998, MNRAS, 301, 478

Thom C. et al., 2012, ApJ, 758, L41

Trayford J. W. et al., 2015, MNRAS, 452, 2879

Tripp T. M. et al., 2011, Science, 334, 952

Trump J. R. et al., 2009, ApJ, 700, 49

Trump J. R. et al., 2015, ApJ, 811, 26

Tumlinson J. et al., 2011, Science, 334, 948

Tumlinson J. et al., 2013, ApJ, 777, 59

Vasiliev E. O., Ryabova M. V., Shchekinov Y. A., 2015, MNRAS, 446, 3078

Vogelsberger M., Genel S., Sijacki D., Torrey P., Springel V., Hernquist L., 2013, MNRAS, 436, 3031

Werk J. K., Prochaska J. X., Thom C., Tumlinson J., Tripp T. M., O'Meara J. M., Meiring J. D., 2012, ApJS, 198, 3

Werk J. K., Prochaska J. X., Thom C., Tumlinson J., Tripp T. M., O'Meara J. M., Peeples M. S., 2013, ApJS, 204, 17

Werk J. K. et al., 2016, ApJ, 833, 54

Wiersma R. P. C., Schaye J., Smith B. D., 2009, MNRAS, 393, 99

APPENDIX A: RESOLUTION TEST

We examine the *M4.4* runs with 8 × higher mass resolution. The No-AGN-Rad-*M4.4* run in Fig. A1 has 0.17 dex higher columns than the *M5.3* resolution run, but the O VI columns remain nearly a factor of 2 too low. Opp16 (section 6.1) argued that the shortfall in simulated O VI might be rectified by reducing the feedback efficiency to form more stars and hence synthesize more oxygen, but this clearly does not work. Our *M4.4* run has an 0.30 dex higher stellar mass than the EAGLE-Recal prescription *M4.4* in Opp16, but the O VI is nearly the same level as this previous run.

The *L441d10t6-M4.4* and *L441d10t5-M4.4* runs listed in Table 2 show milder (≈2/3rd as strong) increases in O VI due to the PZF effect, but *L441d10t5-M4.4* provides an excellent fit to the COS-Halos data, and closely follows the *L441d10t5* model in Fig. A1 (cf. maroon dotted and green dashed lines). The smaller PZF effect at higher resolution owes to the weaker feedback that our *M4.4* model uses, leaving CGM metals at a slightly higher density, and reducing the strength of the PZF effect due to shorter recombination times.
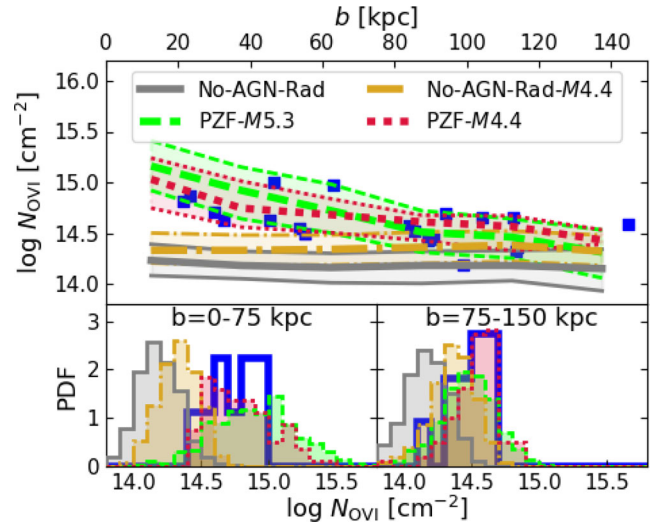

Figure A1. SMOHALOS realizations are plotted as in Fig. 2 using $t_{AGN} = 10^5$ yr models (*L441d10t5*) for the fiducial *M5.3* resolution and the 8 × higher *M4.4* mass resolution models.

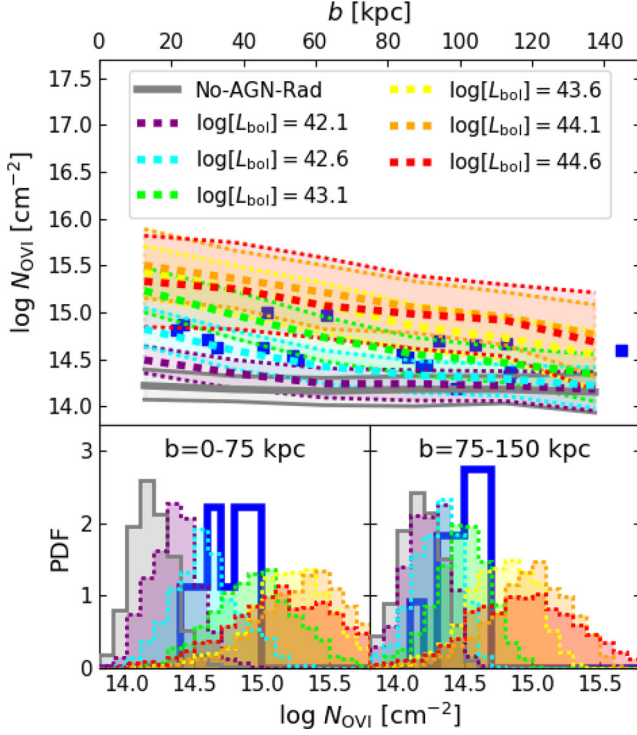**Figure B1.** SMOHALOS realizations are plotted as in Fig. 2, using constant AGN-on models. Increasing AGN radiation increases O VI column density.

APPENDIX B: AGN-ON MODELS

The effect of constant AGN irradiation is demonstrated in Fig. B1 using the fiducial *M5.3* resolution. Six AGN-on models are shown increasing from $L_{bol} = 10^{42.1}$ to $10^{44.6}$ erg s^{-1} in steps of 0.5 dex. All models show an increase over the No-AGN-Rad model. These models are more applicable to cases when the AGN is observed to be on as in the COS-AGN observing programme (Berg et al. in preparation). The $L_{bol} = 10^{43.1}$ erg s^{-1} model has the same time-averaged s$\dot{M}_{BH} = 2.5 \times 10^{-10}$ yr^{-1} as the *L441d10t5* model, and almost exactly replicates its O VI statistics, since that PZF model is in the limit of AGN interval times $\ll t_{rec}$ where the column densities approach the steady state of constant ionization by the AGN+EGB field.

The increase of O VI saturates above $L_{bol} \approx 10^{43.6}$ erg s^{-1}, because the AGN begins to ionize more oxygen to higher levels (O VII through O IX). Even higher AGN luminosities than those explored here (i.e. in the realm of proper quasars) will result in less O VI than these peak models (OS13).

This paper has been typeset from a T$_E$X/L^{A}T$_E$X file prepared by the author.